AD-A103 060 LUTECH INC BERKELY CA F/G 20/14
A STUDY OF NON-TEM MODE SUPPRESSION IN PARALLEL-PLATE TYPE OF E--ETC(U)
MAR 81 D V GIRI F29601-78-C-0080
UNCLASSIFIED AFWL-TR-80-108 NL

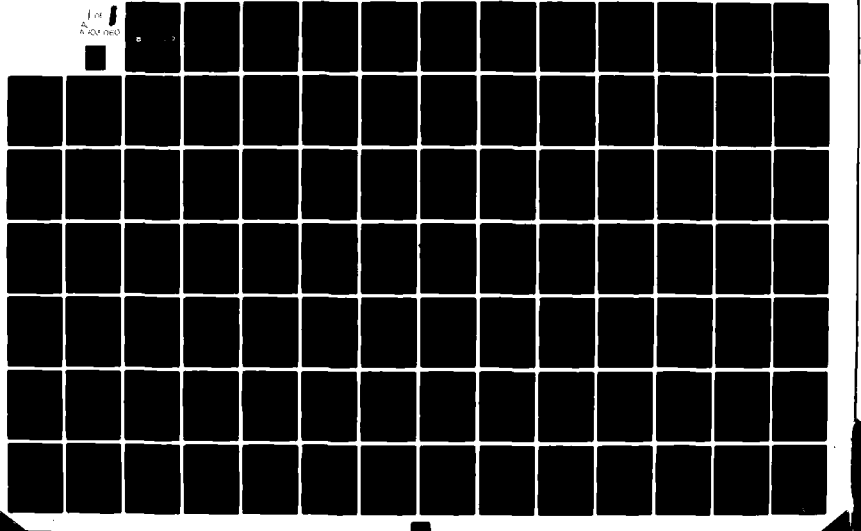

AFWL-TR-80-108

LEVEL II

AFWL-TR-80-108

A STUDY OF NON-TEM MODE SUPPRESSION IN PARALLEL-PLATE TYPE OF EMP SIMULATORS

D. V. Giri

LuTech, Inc.
Berkeley, CA 94701

March 1981

Final Report

Approved for public release; distribution unlimited.

AIR FORCE WEAPONS LABORATORY
Air Force Systems Command
Kirtland Air Force Base, NM 87117

This final report was prepared by LuTech, Incorporated, Berkeley, California, under Contract F29601-78-C-0080, Job Order 12090606 with the Air Force Weapons Laboratory, Kirtland Air Force Base, New Mexico. Dr Michael G. Harrison (NTYE) was the Laboratory Project Officer-in-Charge.

When US Government drawings, specifications, or other data are used for any purpose other than a definitely related Government procurement operation, the Government thereby incurs no responsibility nor any obligation whatsoever, and the fact that the Government may have formulated, furnished, or in any way supplied the said drawings, specifications, or other data, is not to be regarded by implication or otherwise, as in any manner licensing the holder or any other person or corporation, or conveying any rights or permission to manufacture, use, or sell any patented invention that may in any way be related thereto.

This report has been authored by a contractor of the United States Government. Accordingly, the United States Government retains a nonexclusive, royalty-free license to publish or reproduce the material contained herein, or allow others to do so, for the United States Government purposes.

This report has been reviewed by the Public Affairs Office and is releasable to the National Technical Information Service (NTIS). At NTIS, it will be available to the general public, including foreign nations.

This technical report has been reviewed and is approved for publication.

Michael G Harrison

MICHAEL G. HARRISON, PhD
Project Officer

FOR THE COMMANDER

J. Philip Castillo

J. PHILIP CASTILLO, PhD
Chief, Electromagnetics Branch

Norman K. Blocker

NORMAN K. BLOCKER
Colonel, USAF
Chief, Applied Physics Division

DO NOT RETURN THIS COPY. RETAIN OR DESTROY.

UNCLASSIFIED

SECURITY CLASSIFICATION OF THIS PAGE (When Data Entered)

REPORT DOCUMENTATION PAGE

READ INSTRUCTIONS BEFORE COMPLETING FORM

1. REPORT NUMBER	2. GOVT ACCESSION NO.	3. RECIPIENT'S CATALOG NUMBER
AFWL-TR-80-108	AD-A103066	

4. TITLE (and Subtitle)
A STUDY OF NON-TEM MODE SUPPRESSION IN PARRALLEL-PLATE TYPE OF EMP SIMULATORS

5. TYPE OF REPORT & PERIOD COVERED
Final Report

6. PERFORMING ORG. REPORT NUMBER

7. AUTHOR(s)
D. V. Giri

8. CONTRACT OR GRANT NUMBER(s)
F29601-78-C-0080

9. PERFORMING ORGANIZATION NAME AND ADDRESS
LuTech, Inc.
Berkeley, CA 94701

10. PROGRAM ELEMENT, PROJECT, TASK AREA & WORK UNIT NUMBERS
64747F/12090606

11. CONTROLLING OFFICE NAME AND ADDRESS
Air Force Weapons Laboratory (NTYE)
Kirtland Air Force Base, NM 87117

12. REPORT DATE
March 1981

13. NUMBER OF PAGES
94

14. MONITORING AGENCY NAME & ADDRESS (if different from Controlling Office)

15. SECURITY CLASS. (of this report)
Unclassified

15a. DECLASSIFICATION/DOWNGRADING SCHEDULE

16. DISTRIBUTION STATEMENT (of this Report)
Approved for public release; distribution unlimited.

17. DISTRIBUTION STATEMENT (of the abstract entered in Block 20, if different from Report)

18. SUPPLEMENTARY NOTES

19. KEY WORDS (Continue on reverse side if necessary and identify by block number)
Mode Suppression
Parallel-Plate Simulators
Modal Filter
Resistive Sheet

20. ABSTRACT (Continue on reverse side if necessary and identify by block number)
The subject of this report is the suppression or damping of non-TEM modes in the transmission-line type of EMP simulators. This suppression may be accomplished by introducing a spatial modal filter (SMF), initially in the output conical section of the model simulator. In this report we deal with the electromagnetic considerations of the SMF, which is essentially decoupled from the principal TEM mode. Although somewhat incomplete, the available experimental results performed on the model simulator are included.

DD FORM 1 JAN 73 1473

UNCLASSIFIED

SECURITY CLASSIFICATION OF THIS PAGE (When Data Entered)

PREFACE

I am thankful to Dr. Carl E. Baum for suggesting this problem and for many useful discussions. Prof. R.W.P. King and his colleagues have contributed significantly to our understanding of the incident field in the simulator, in terms of two-parallel plate modes. The experimental work relevant to this project is currently on-going under a separate effort at Harvard University. However, the experimental work reported in their monthly progress reports is included in this report with their kind permission. Thanks are also due to Drs. K.C. Chen, M.G. Harrison, M. Bradshaw and Mr. W. Kehrer for their encouragement and interest in this problem.

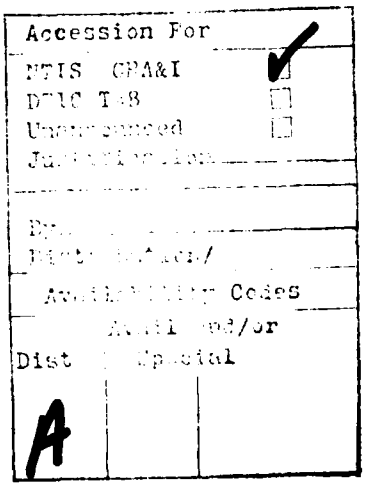

CONTENTS

ILLUSTRATIONS

ILLUSTRATIONS (cont.)

ILLUSTRATIONS (cont.)

TABLES

I. INTRODUCTION

An important class of electromagnetic pulse (EMP) simulators is the parallel-plate transmission-line type. This type of electromagnetic structure is essentially an open waveguide, between the conductors of which a transient pulse with a planar wavefront must travel. In practice, however, the fields obtained in the working volume can depart from the ideal transverse electromagnetic (TEM) behavior owing to the excitation and propagation of non-TEM modes. It has been known for some time (Refs. 1 through 5) that a finitely wide parallel-plate transmission line can support and propagate transverse electric (TE) and transverse magnetic (TM) modes if they are excited for any reason. Since the chief object of such an EMP simulator is to produce an EMP environment appropriate to a plane wave (outside the source region), it is desirable to suppress the non-TEM modes without disturbing the TEM wave. To successfully accomplish this suppression, a clear understanding of the characteristics of the TEM and non-TEM (i.e., TE and TM) modes is essential. Much detailed work has been done concerning the TEM properties of both the parallel-plate (Refs. 6 through 9) and the conical (Refs. 10 and 11) transmission lines. References 12 and 13 have considered the conical transmission line as a launcher and receptor of waves on the cylindrical transmission line by introducing the concept of dispersion distances, or equivalently, dispersion times. Formulas have also been developed (Ref. 13) for the TEM mode coefficient in terms of the cross-section fields. Detailed calculations of TE and TM modes of propagation are currently available for the two limiting cases of narrow (separation >> width)(Ref. 1) and wide (separation << width)(Refs. 4 and 5) plates. More recently, a parametric study (Ref. 14) has been completed for the general case where the separation-to-width ratio is not restricted. This study has considered geometries of the existing (ALECS, ARES, and ATLAS I) and future (ATLAS II) transmission-line

type of EMP simulator facilities at the Air Force Weapons Laboratory (AFWL), as well as the laboratory model simulator at Harvard University. This study has indicated that the field distributions in the transverse direction are fairly uniform, indicating that to understand the incident fields in the simulator, it is adequate to use the propagating modes of two parallel plates that are infinitely wide. Some of the experimentally detected performance defects are attributable to the existence of non-TEM modes. All of these considerations point out a need to suppress or dampen the non-TEM modes.

In Section II, the departure of the measured fields in the working volume from the ideal TEM behavior are considered, and in Section III, available computations of TE and TM modes in the parallel-plate region are reviewed. Sections IV and V deal with various aspects of the spatial modal filter and design formulas are developed. In Section VI, a specific design is carried out and methods of evaluating the spatial modal filter are suggested. Section VII deals with the experimental work on mode suppression. The report concludes with a summarizing Section VIII.

II. DEPARTURE FROM THE IDEAL TEM BEHAVIOR

This class of EMP simulators operating in a pulsed mode is a complex electromagnetic structure to analyze. This complexity is partially because of the fact that the input pulse contains a wide range of frequencies and, consequently, the relevant dimensions of the structure ranges from a small fraction of a wavelength to many wavelengths. Because of this the simulator, while operating in a pulsed mode, is a transmission line, a radiator, and an optical diffracting structure; all for the same pulse. In Reference 15 the electromagnetic characteristics of the simulator were qualitatively discussed by categorizing the frequency range of interest into (a) low frequencies, (b) high-frequency asymptotics, and (c) intermediate frequencies.

At low frequencies, one has near-ideal conditions in terms of simulation because quasi-static considerations apply and the TEM mode of propagation is dominant. The main problem is to minimize the impedance discontinuity and TEM field discontinuity across the junction between the cylindrical and the conical transmission lines. Such a matching of the TEM modes at the input and output bends is achieved by reducing the dispersion distance (Refs. 12 and 13).

At higher frequencies, the relevant dimensions of the simulator, e.g., width and spacing of the plate become several wavelengths long, and ray-optical considerations apply. Several canonical problems have been defined and solved (Refs. 16 through 19), which are useful in estimating the early-time pulsed fields associated with conducting wedges and thus reduce waveform distortion. Some experimentally measured data (Ref. 20) are available concerning the early-time fields indicating the $(1/r)$ variation of the spherical wave launched by the conical line followed by edge diffraction and specular

reflections. Some of the problems are large dispersion times, edge diffractions, and excessive ripple in the measured data.

However, it is the intermediate frequencies that present the most serious problems. Relevant distances now become comparable to wavelengths rendering both the quasi-static and the ray-optic considerations inapplicable. This report focuses attention on the behavior of the simulated electromagnetic fields in this frequency regime by taking a superposition of the TEM and non-TEM modes. The non-TEM modes are those supported in an infinitely wide, two-parallel-plate open waveguiding structure, which are to be contrasted with the familiar propagating modes of a closed rectangular waveguide or a closed circular coaxial transmission line. By taking this view, one can define the problem to be that of damping or suppressing the non-TEM modes without significantly disturbing the desired TEM mode of propagation.

A typical geometry of this class of EMP simulator is shown in Figure 1. This figure shows a vertically polarized parallel-plate transmission-line type of simulator. By virture of symmetry and practicality, it suffices to construct the symmetric half of the structure above the horizontal symmetry plane where a wide conducting plane is placed. Accordingly, Figure 1 shows the side view of the simulator comprising the top plate of width 2a at a height b above the ground plane. The plate-to-plate separation (for a symmetric situation with two identical parallel plates) is then 2b and the lengths of the conical and the parallel-plate transmission lines are designated L and w, respectively. With reference to this figure, the nonzero components of the electric and magnetic fields for the various modes of propagation in the parallel-plate transmission-line region are:

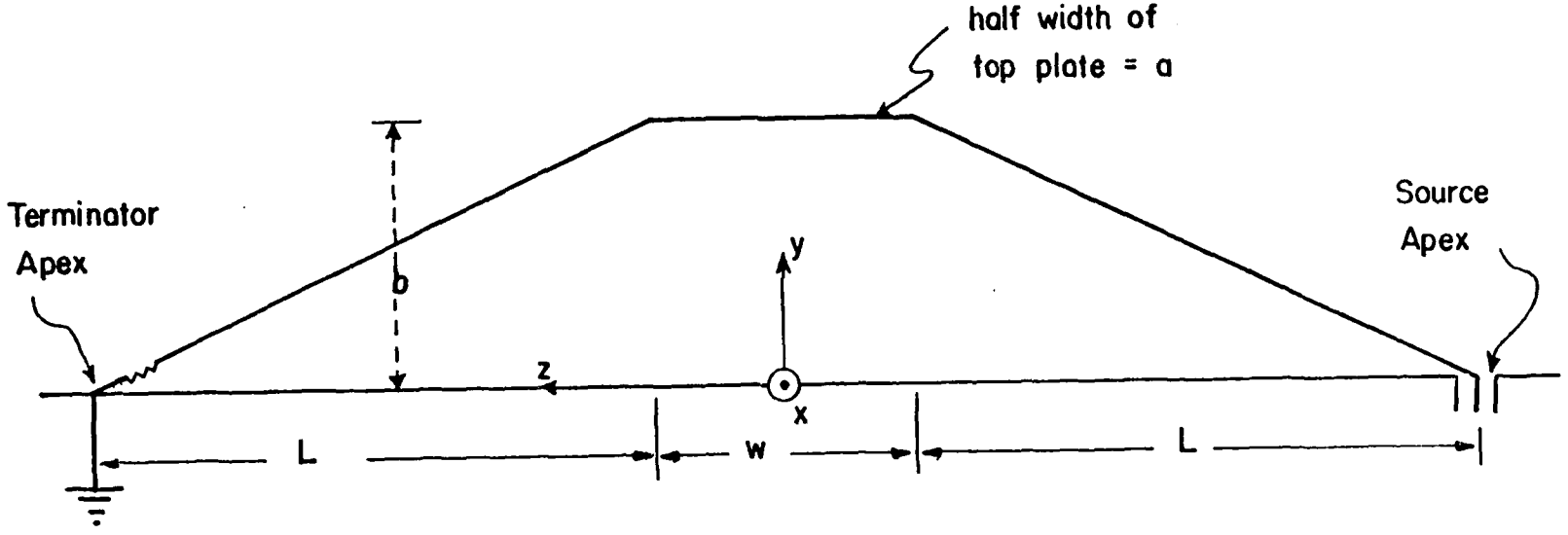

Figure 1. Geometry of a vertically polarized, two-parallel plate transmission-line type of EMP simulator.

(a) TEM mode

$$\tilde{E}_x \ , \ \tilde{E}_y \ , \ \tilde{H}_x \ , \ \tilde{H}_y \qquad \text{with} \quad \tilde{E}_z = \tilde{H}_z = 0$$

(b) TM mode (E mode)

$$\tilde{E}_z, \ \tilde{E}_x \ , \ \tilde{E}_y \ , \ \tilde{H}_x \ , \ \tilde{H}_y \qquad \text{with} \quad \tilde{H}_z = 0$$

(c) TE mode (H mode)

$$\tilde{H}_z, \ \tilde{H}_x \ , \ \tilde{H}_y \ , \ \tilde{E}_x \ , \ \tilde{E}_y \qquad \text{with} \quad \tilde{E}_z = 0$$

All of the above field quantities are functions of position in the transverse plane and frequency. Now, to summarize certain measurements made in the ALECS facility that are relevant in terms of identifying the departure from the ideal TEM behavior. Continuous wave (CW) measurements (Ref. 21) made in the working volume of the ALECS facility have detected what has been referred to as the notch problem. Specifically, the transfer function from the input voltage to the measured fields, when appropriately normalized and plotted as a function of frequency, displays significant notches at certain frequencies. For example, Figure 2 shows the magnitude of the normalized transverse magnetic field H_x measured at the center (0,0,0) and the notch is seen to appear at ~25 MHz, with roughly a ±30% ripple at higher frequencies. Figure 3 is the normalized principal electric field E_y measured at the same location. Note that the principal electric field does not display a notch behavior at the same location, but perhaps a small enhancement. The experimental measurements in the scale model simulator at Harvard University have reproduced the notch behavior in the field quantities. The description of the experimental setup along with the measured fields in the model simulator are well documented in References 22 and 23. Some highlights of

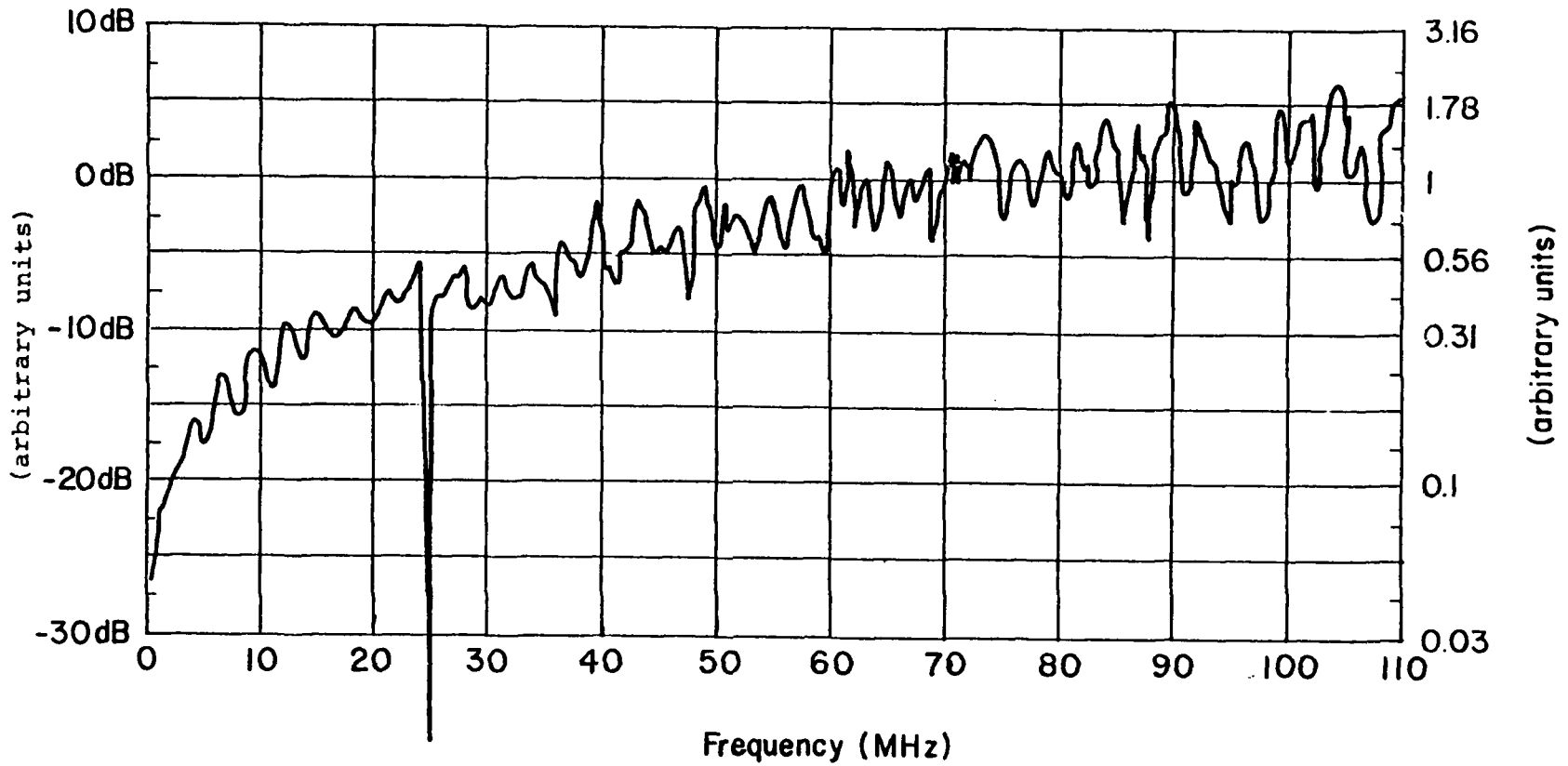

Figure 2. Measured $|\dot{B}_x/\text{constant}|$ at the center with coordinates (0,0,0) in ALECS facility. This figure is reproduced here from Reference 21.

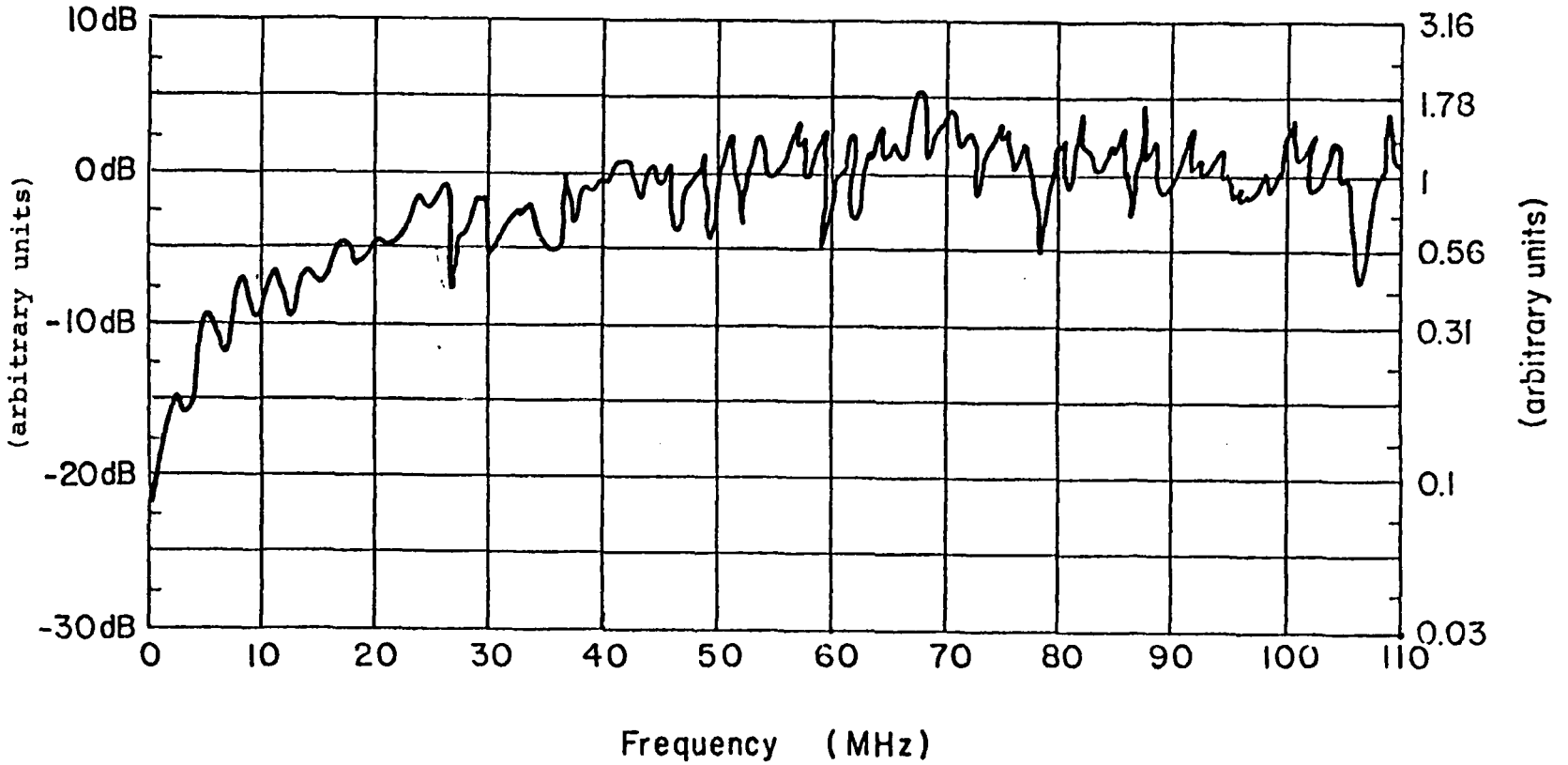

Figure 3. Measured $|\dot{D}_y$ constant| at the center with coordinates (0,0,0) in the ALECS facility. This figure is reproduced here from Reference 21.

the experimental setup of the model simulator along with sample measured fields are reported later in this section. A preliminary measurement of the transverse magnetic field as a function of frequency at a fixed location of (0,0,0) was provided by Blejer (Ref. 24) and is shown in Figure 4. This measurement also displays a sharp null in the magnetic field $\sim$ 264 MHz at the measurement location. The null is caused by a cancellation of the transverse magnetic field of the principal TEM mode by that of the first TM mode, and the frequency of 264 MHz on the model simulator corresponds very closely to the $\sim$ 25 MHz observed in the ALEC facility. Because of non-ideal temrination, the TEM mode and the TM_{01} mode travel in both positive and negative z directions. Furthermore, in both configurations (ALECS and the model simulator), the frequencies where one would expect a higher order mode to be excited corresponds approximately to the relevant dispersion distance d becoming equal to a half wavelength. Considering a direct path from source apex to load apex and another signal path along the edge of the top plate, d is given by

$$d = \frac{\lambda}{2} \cong 2\left[\sqrt{b^2 + a^2 + L^2} - L\right] \qquad (1)$$

where λ is the wavelength corresponding to a frequency where one may expect a higher order TM mode excitation, and the other variables in Equation (1) are illustrated in Figure 1. By substituting the values for the various dimensions, one finds that the frequency of expected excitation of higher TM modes is $\sim$ 25 MHz for ALECS and $\sim$ 256 MHz for the model simulator at Harvard. These compare well with the experimentally observed values of $\sim$ 24 MHz for ALECS and $\sim$ 264 MHz for the model simulator. It can be argued that the notch is due to the superposition of the TEM mode and higher order TM modes. Since the non-TEM modes are evanescent at either end of the simulator,

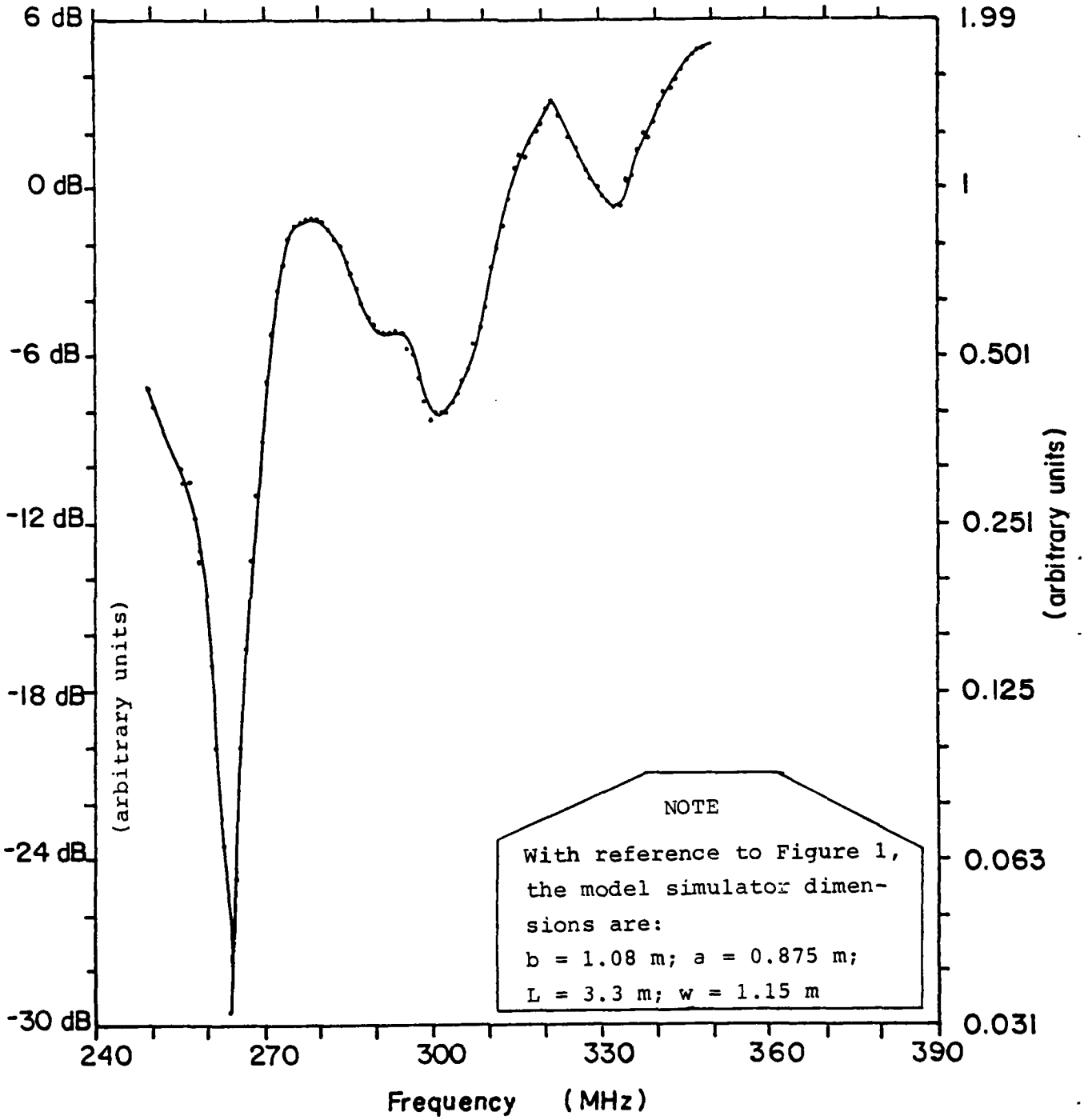

Figure 4. Measured $|B_x/\text{constant}|$ at (0,0,0) in the model simulator at Harvard (Ref. 24).

as expected, all of the input impedance measurements are dominated by the principal TEM mode. Based on these observations, one may conclude that the notch occurs at the center (0,0,0) due to the symmetry in the simulator as a result of near cancellation of the magnetic field of the TEM mdoe with its counterpart in the first TM mode traveling in two directions. A near cancellation in the electric field at the same location is not expected for the following reasons. The dominant TEM mode is partially a standing wave because of the output bend and nonideal termination, whereas the TE and TM modes are standing waves owing to reflections. The magnetic field (H_x component) in the TM modes propagating in the positive and negative z directions add and their sum cancels the H_x of the principal TEM mode resulting in the notch behavior. However, the electric field in the TM modes propagating in the positive and negative z directions cancel from each other and thus one does not expect a notch at (0,0,0) in the electric field. This is consistent with the experimentally measured electric field (E_y) data shown in Figure 3. Furthermore, near the top plate both H_x and E_y in the TM mode will have the reversed sign from their values at the ground plane, leading to no cancellation in either of these field quantities with their counterparts in the TEM mode. Also note that the frequency where the notch occurs is also predictable from the dispersion times/distances calculations.

The remainder of this section deals with the incident field measurements on the model simulator at two frequencies, 626.5 and 264 MHz, corresponding roughly to 60 and 25 MHz on the ALECS facility. The object of reviewing these measurements is to show that the incident field can indeed be thought of as a superposition of TEM and a finite number of TM_{on} modes traveling in two directions.

1. The Harvard EMP Simulator

A detailed experimental study has been made of the electric field in the guided-wave simulator shown schematically in Figures 5 and 6. The simulator consists of a rectangular metal plate between sloping triangular plates supported over a large aluminum ground plane (7.93 × 3.35 m) by dielectric cables and styrofoam blocks. It is driven at one end by the vertical extension of the inner conductor of a coaxial line connected to a CW power oscillator. The simulator is terminated at the other end in standard 2-W resistors in parallel. The three-dimensional region under the rectangular plate is where the fields have been mapped. The length ℓ of the simulator is 115 cm, and its width 2a is 175 cm. Its height b above the ground plane is adjustable with the help of hinged joints between it and the sloping triangular plates combined with movable feed and load points. Two heights and frequencies have been used. They are $b = 108$ cm with $f = 625$ MHz or $\lambda = 48$ cm so that $b/\lambda = 2.25$, and $b = 75$ cm with $f = 264$ MHz or $\lambda = 113.6$ cm so that $b/\lambda = 0.66$. The length of each of the identical triangular plates is 331 cm; their projections on the ground plane when $b = 108$ cm, are 311.5 cm; when $b = 75$ cm, the projections are 322 cm. These dimensions provide a characteristic impedance of 100 Ω when $b = 108$ cm; of 80 Ω when $b = 75$ cm. A small corner reflector is placed behind the driven end; absorbing material completely surrounds the edges of the ground plane.

Cartesian coordinates are used to describe the location of a point in and near the working volume of the simulator. The origin is on the ground plane directly below the center of the parallel plate. The unit vectors $\vec{1}_x$, $\vec{1}_y$, $\vec{1}_z$ define, respectively, the transverse, vertical, and longitudinal directions, as indicated in Figure 6. Note that $\vec{1}_z$ points in the direction of propagation. For preliminary measurements

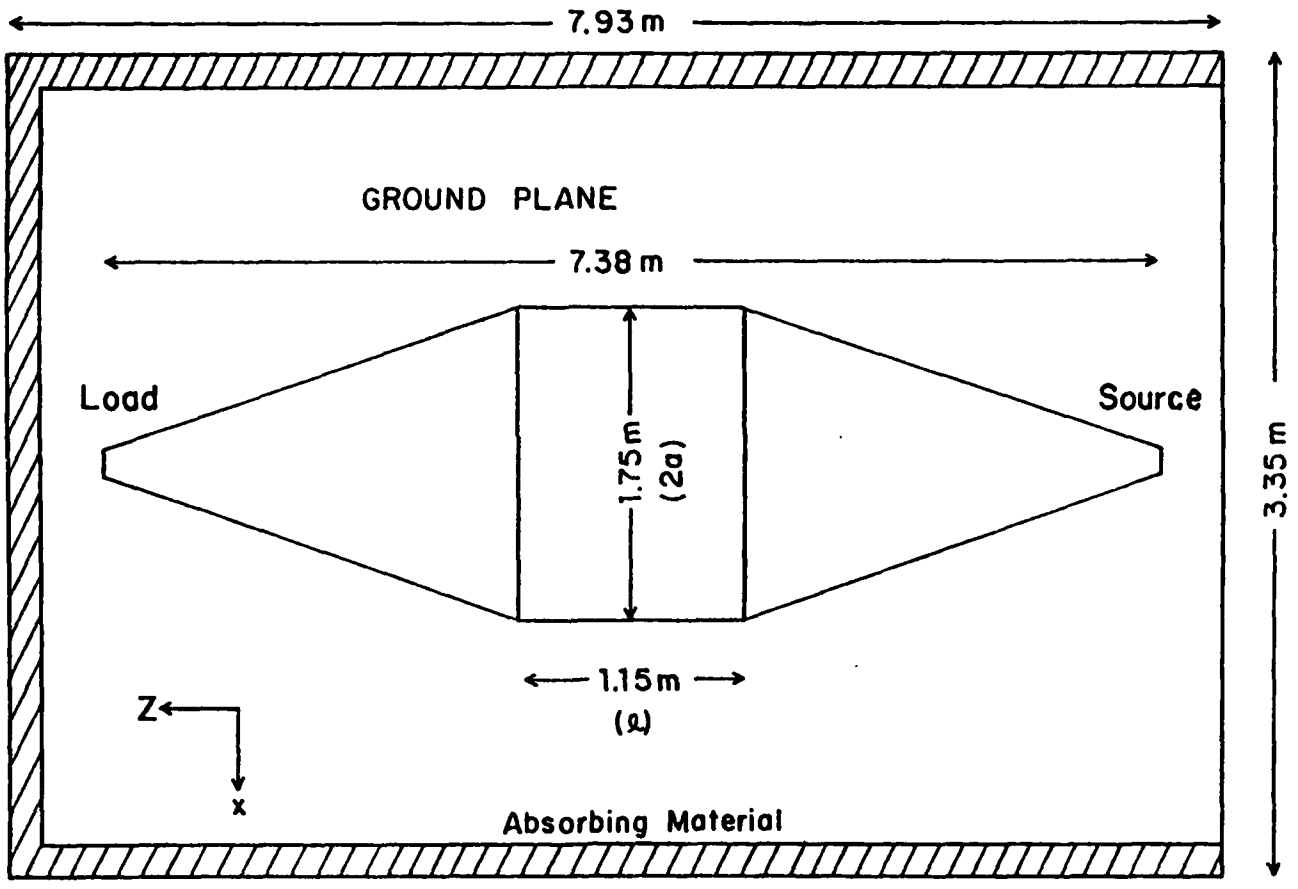

Figure 5. Top view of simulator setup.

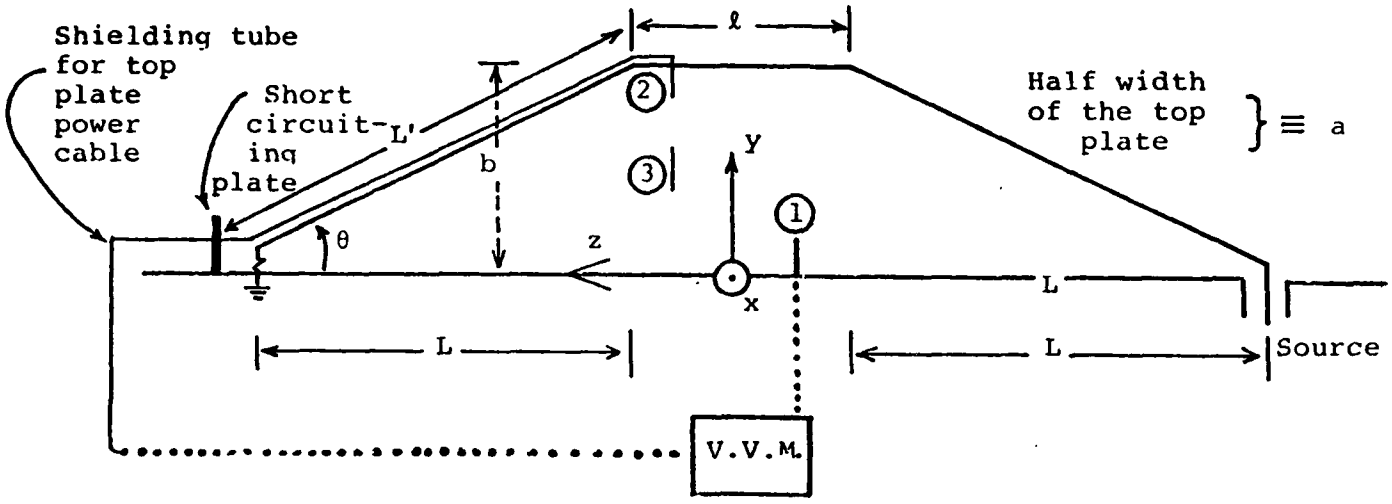

Figure 6. Simulator with (1) ground-plane probe, (2) top-plate probe, and (3) space probe in the parallel plate region. The dimensions are L = 3.11 m, L' = 3.31 m, ℓ = 1.15 m, a = 0.875 m, and b = 1.08 m and 0.75 m.

the spherical coordinates (r,θ,ϕ) are also used with the origin ($r = 0$) on the ground plane at the driving point. When $b = 108$ cm, the load is at $(r,\phi,\theta) = (738,90°,0°)$, where r is in centimeters.

In order to determine the electric field in the parallel plate region and in the adjacent conical sections as well as along the surfaces of the ground plane and the upper parallel plate, a system of movable probes was designed and constructed for the direct measurement of both the amplitude and phase of E_z and E_y. As explained later, a small component E_x exists primarily near the open sides where fringing occurs, but this could not be measured. The component E_y on the ground plane was measured with a monopole probe, 4 cm long, mounted on a brass disk 10 cm in diameter and designed to slide along the ground plane when moved by means of a pulley system. The probe cable was constrained to lie flat on the ground plane and was, therefore, always perpendicular to the electric field. The measurement of E_y on the underside of the upper parallel plate was accomplished with a monopole probe that projects down into the parallel plate region through longitudinal slots cut into the parallel plate. The probe was mounted on a brass block which was machined to slide in the slots. The output cable from the base of the probe was placed in a shielding tube constructed to lie along the upper surface of the sloping triangular plate leading to the load. The cable in its shielding tube extended beyond the load parallel to the ground plane and over its edge to the instrumentation below, as shown in Figure 6. The section over the ground plane constituted a transmission line with a characteristic impedance of 100 Ω. It was short-circuited at a distance of $\lambda/4$ from the load by a metal plate and so acted like an open circuit at the load.

The electric field throughout the parallel plate region was measured with a dipole antenna that could be oriented vertically to measure E_y and horizontally to measure E_z. It was continuously movable in the parallel plate region and adjacent sections below the conical plates. The probe cable consisted of twin coaxial lines that were held parallel to the transverse x-axis as the probe was moved. This assured that the coaxial lines were perpendicular to both E_z and E_y, but necessarily parallel to E_x -- which could excite axial standing-wave distributions of current and charge on their surfaces. Since the standing wave distributions would have a charge maximum at the end adjacent to the terminals of the dipole, they could induce an undesired voltage across the terminals if complete geometrical symmetry was not present. No such difficulty was encountered with f = 625.5 MHz and a simple space probe (Ref. 24) was used to measure E_z and E_y throughout the parallel plate region. At f = 264 MHz, an undesired voltage due to E_x was observed -- presumably because the long twin cable from the probe in the working volume to the vector voltmeter under the ground plane happended to be near a resonant length. This difficulty was avoided with an adjustable extension beyond the dipole. When the extension was adjusted to a quarter wavelength, the dipole was located at a charge minimum instead of a charge maximum in any standing wave induced on the tube by E_x. The undesired voltage across the terminals of the evidently not perfect symmetrical dipole was thus reduced to a nonobservable value.

Before measurements were made in the model simulator, the standing-wave pattern on the ground plane with its surrounding absorbing walls was investigated. These tests indicated that

the reflections that produce the small standing wave originate at the rear edge and wall of the absorbing material. Their small amplitude shows that while there is some reflection from the edge of the ground plane and the absorbing material, this latter is generally effective in providing a predominantly traveling wave that closely approximates that over a plane of infinite extent.

The next set of preliminary measurements was carried out with the parallel rectangular and sloping triangular plates of the simulator in place and with a load of 105Ω as the termination. This value was chosen after measurements showed that it provided the lowest standing-wave ratio in the region near the load. Graphs of $|E_y|$ and $|\theta_y|$ are shown in Figure 7 for a distance of more than a wavelength adjacent to the 105Ω load. The standing-wave ratio of 3.7 shows that there is substantial reflection even with the matched load at this frequency of 626.5 MHz. This is consistent with the independent terminator study (Ref. 25) which concluded that at high frequencies, an inductive termination is needed to effectively minimize reflections.

In conclusion, the main outline is that of a traveling spherical wave in the input conical region which transforms into a traveling plane wave in the parallel plate region (- different set of coordinate reference) with a superimposed reflected wave of relatively small amplitude.

2. THE FIELD IN THE PARALLEL-PLATE SECTION; TEM AND TM MODES

Since the field incident on the parallel-plate section of the simulator is a spherical wave from the input conic section, it is of interest to determine the nature of the phase fronts which characterize the electromagnetic field in that section. Measured graphs of the wave fronts or countours of constant phase, θ_y = constant, of the vertical component E_y of the

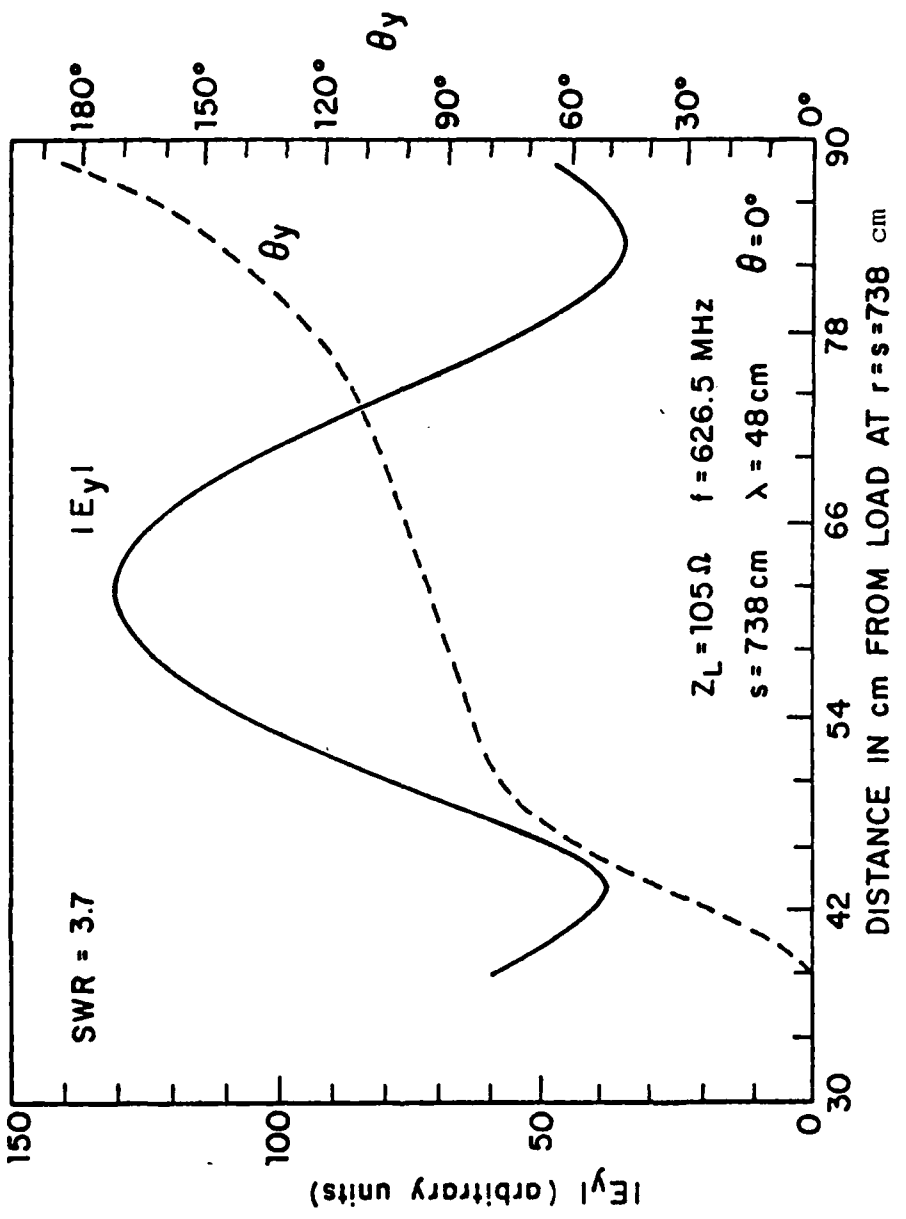

Figure 7. Standing wave of the $|E_y|$ field near load.

field in the parallel-plate region when b = 108 cm and f = 626.5 MHz are shown in Figures 8 and 9 in vertical yz planes at discrete values of x ranging from x = 1.7 cm near the center at x = 0 to x = -70.3 cm near the edge at x = -87.5 cm. Also shown are the wave fronts of a spherical wave originating at the driving point (x = 0, z = -369 cm, y = 0). Clearly the phase fronts throughout the parallel-plate region are essentially spherical with a superimposed oscillation due to reflections from the top plate.

It is not convenient to describe the field in a parallel-plate waveguide in terms of spherical wave fronts originating at an outside point. The natural representation is in terms of a superposition of plane waves known as parallel-plate modes. The simplest form is given by the mode theory of infinite parallel planes (Ref. 26). The TM modes symmetric in y are applicable to the parallel-plate section of the simulator. Using the relevant TM modes* given in Reference 26, one can write the field quantities for the various modes.

For the Harvard working volume and with the operating frequency at f = 626.5 MHz, the TEM mode with n = 0 and three TM_{0n} modes with n = 1,2,3, can propagate. For the TEM mode, $k = k_{g0} = 0.1309\ cm^{-1}$; for the TM_{0n} modes, $k_{g1} = 0.977k = 0.128\ cm^{-1}$, $k_{g2} = 0.893k = 0.117\ cm^{-1}$, and $k_{g3} = 0.748k = 0.098\ cm^{-1}$. The corresponding guide wavelengths

*When referred to the full height with image, b is replaced by 2b, and n = 0,2,4,6,..., instead of 0,1,2,3,... .

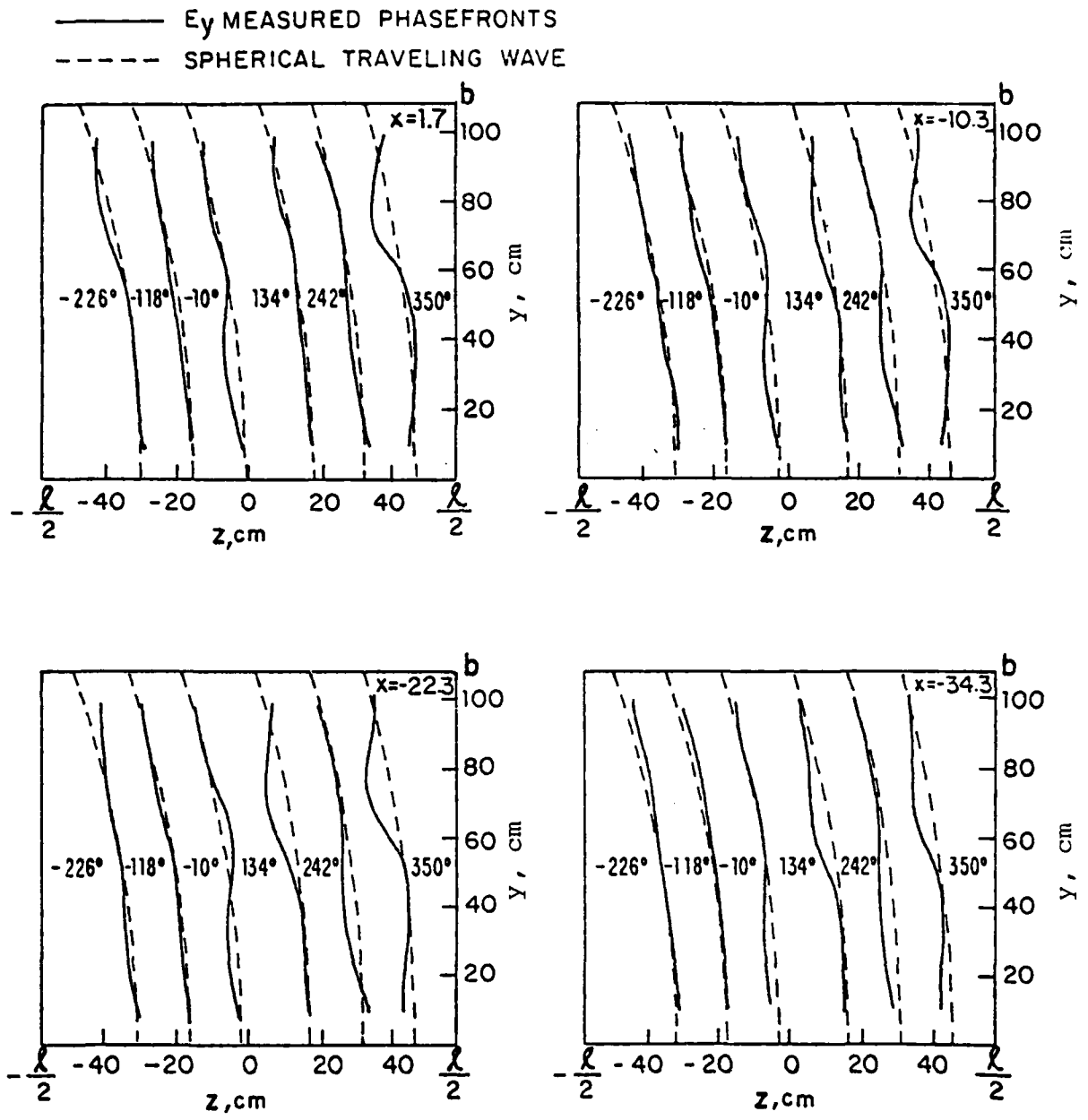

Figure 8. Measured constant phase curves in the working volume; b = 108 cm, ℓ = 114.8 cm and f = 626.5 MHz.

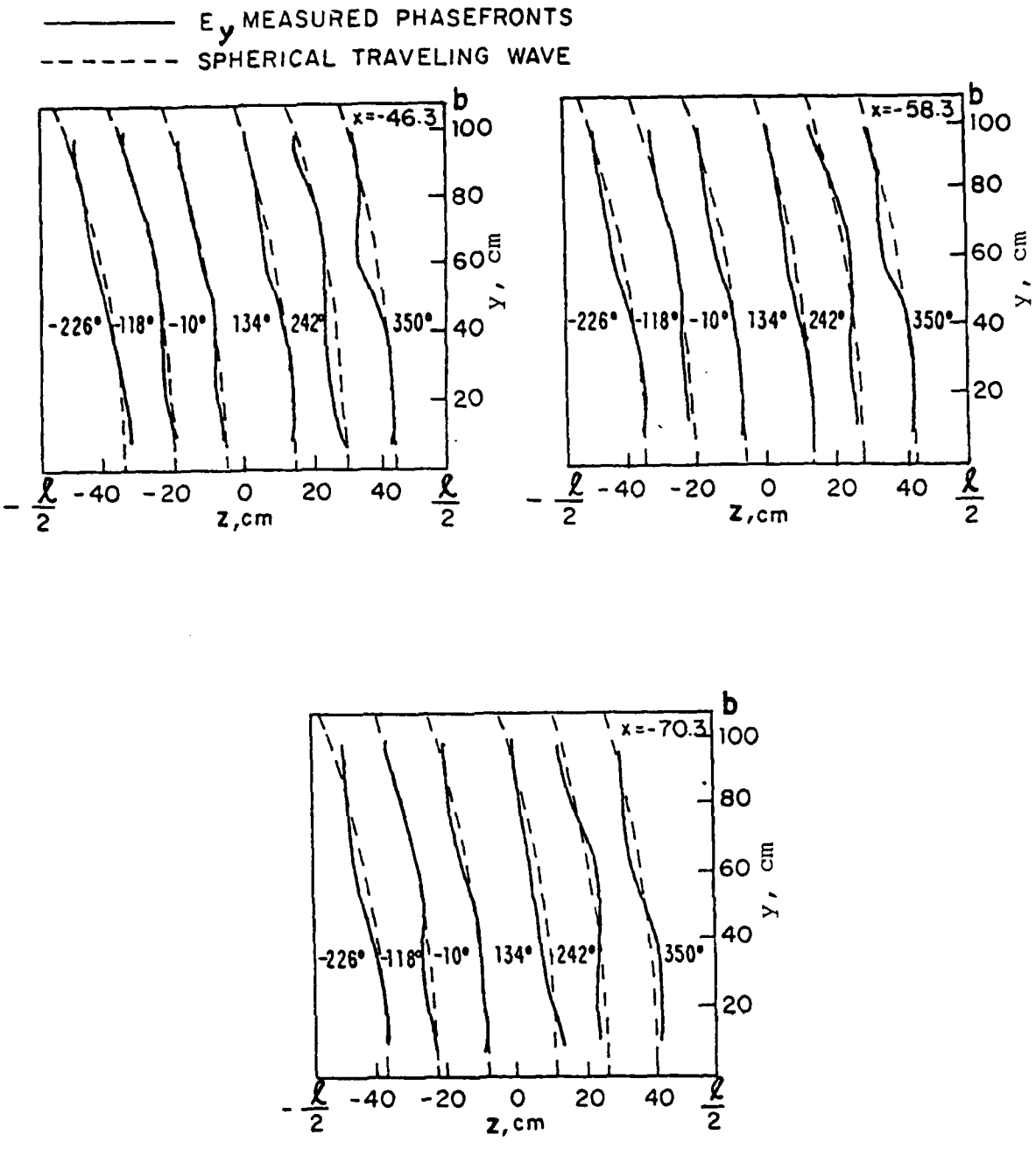

Figure 9. Measured constant phase curves in the working volume; b = 108 cm, ℓ = 114.8 cm, and f = 626.5 MHz.

are $\lambda = \lambda_{g0} = 48$ cm for the TEM mode and $\lambda_{g1} = 49.1$ cm, $\lambda_{g2} = 53.7$ cm, and $\lambda_{g3} = 64.2$ cm for the TM_{0n} modes. The fields for the four modes are:

$$\text{TEM:} \quad E_z = 0, \quad E_y = 0.096V_0(z), \quad H_x = 0.096I_0(z) \tag{2}$$

$$TM_{01}: \quad E_z = -i11.4I_1(z)\sin(0.029y), \quad E_y = -0.136V_1(z)\cos(0.029y)$$

$$H_x = 0.136I_1(z)\cos(0.029y) \tag{3}$$

$$TM_{02}: \quad E_z = -i22.8I_2(z)\sin(0.058y), \quad E_y = -0.136V_2(z)\cos(0.058y)$$

$$H_x = 0.136I_2(z)\cos(0.058y) \tag{4}$$

$$TM_{03}: \quad E_z = -i34.2I_3(z)\sin(0.087y), \quad E_y = -0.136V_3(z)\cos(0.087y)$$

$$H_x = 0.136I_3(z)\cos(0.087y) \tag{5}$$

The relative amplitudes of the incident and reflected waves for each of these modes are not readily determined analytically. However, they can be estimated at any cross section of the parallel plate region by comparison with the measured field.

The electric field lines characteristic of the TEM and first three TM_{0n} modes are shown in the yz-plane in Figure 10. At the upper left are the exclusively vertical field lines of the TEM mode. They have alternate upward and downward maxima at intervals of $\lambda/2 = 24$ cm. Note that there is no associated component E_z. At the upper right are the electric field lines for the TM_{01} mode. These resemble the TEM mode near the top conductor, but are oppositely directed near the ground plane since they are parts of closed loops with an E_z component in the region halfway between the conducting surfaces. The alternating upward and downward maxima now occur at intervals of $\lambda_{g1}/2 = 24.6$ cm. On the lower left are the E-lines for the TM_{02} mode, on the lower right those of the TM_{03} mode. These have additional closed loops in the vertical

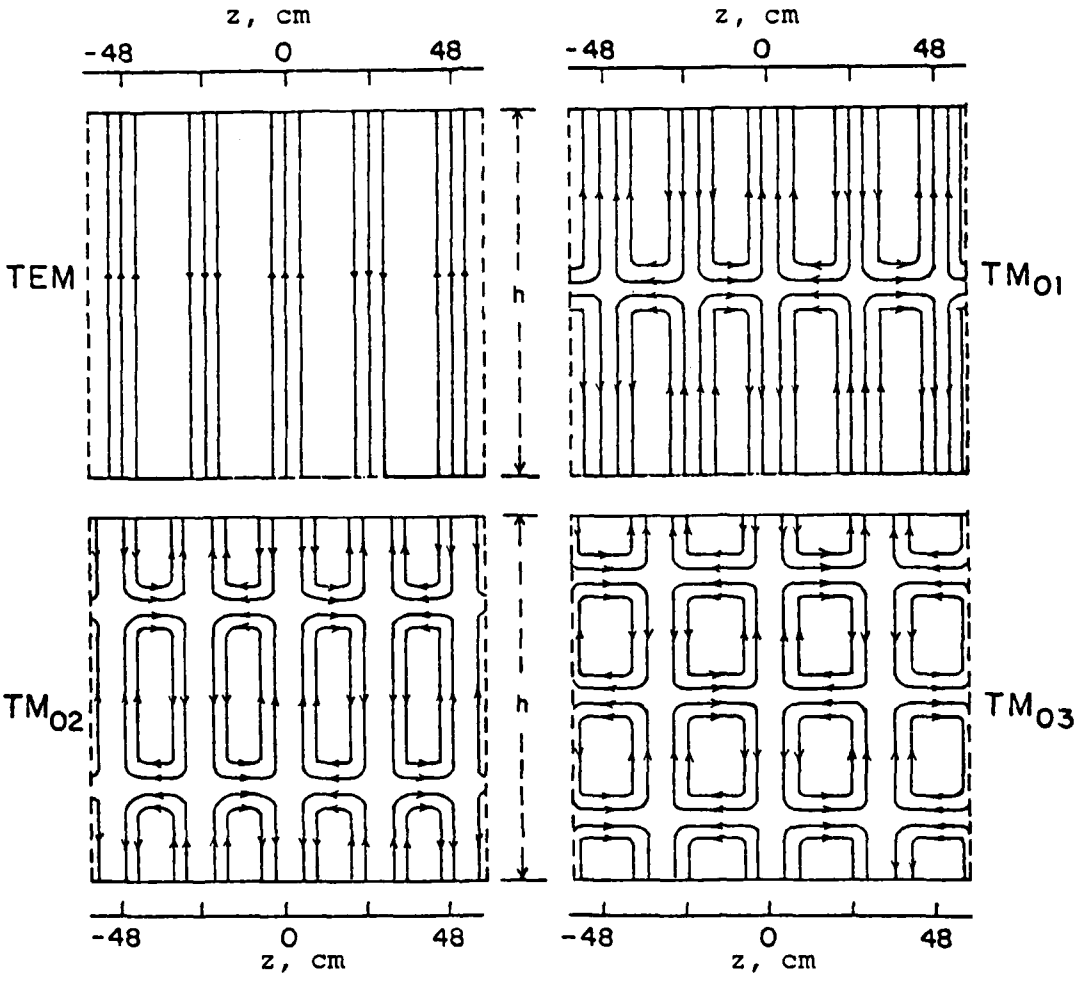

Figure 10. Electric field lines for four parallel-plate modes in working volume λ = 48 cm.

direction with associated E_z- components and a wider spacing between successive maxima in the horizontal direction. Thus, for the TM_{13} mode, the maxima occur at intervals of $\lambda_{g2}/2$ = 26.8 cm and for the TM mode at intervals of $\lambda_{g3}/2$ = 32.1 cm.

When b = 75 cm and f = 264 MHz or λ = 113.6 cm, the only propagating modes are the TEM mode and the TM_{11} mode. For the latter, the cut-off wavelength is λ_{c1} = 2b = 150 cm and the guide wavelength is λ_{g1} = 174 cm.

3. THE MEASURED FIELD IN THE WORKING VOLUME:

<u>b = 2.25λ = 108 cm; f = 626.5 MHz</u>

The principal components, E_y and E_z, of the electric field in the working volume were measured as functions of the longitudinal variable z with the transverse variables x and y as the parameters. Consider first the field with f = 626.5 MHz when b = 108 cm = 2.25λ and λ = 48 cm. (The field with b = 75 cm = 0.66λ with λ = 113.6 cm is studied in the next subsection.)

Figure 11 shows the measured distributions of $|E_y|$ and $|E_z|$ in the yz-plane at x = 1.7 cm, i.e., very near the central plane x = 0 of the parallel-plate region. The parameter y/b ranges from 0 at the bottom to y/b = 1 at the top. The field along the ground plane y/b = 0 was measured with the monopole probe mounted on the movable metal disk. The field along the underside of the top plate was measured with the monopole probe that moves in the longitudinal slots. The field at all other values of y/b was measured with the movable dipole space probe that is supported by a

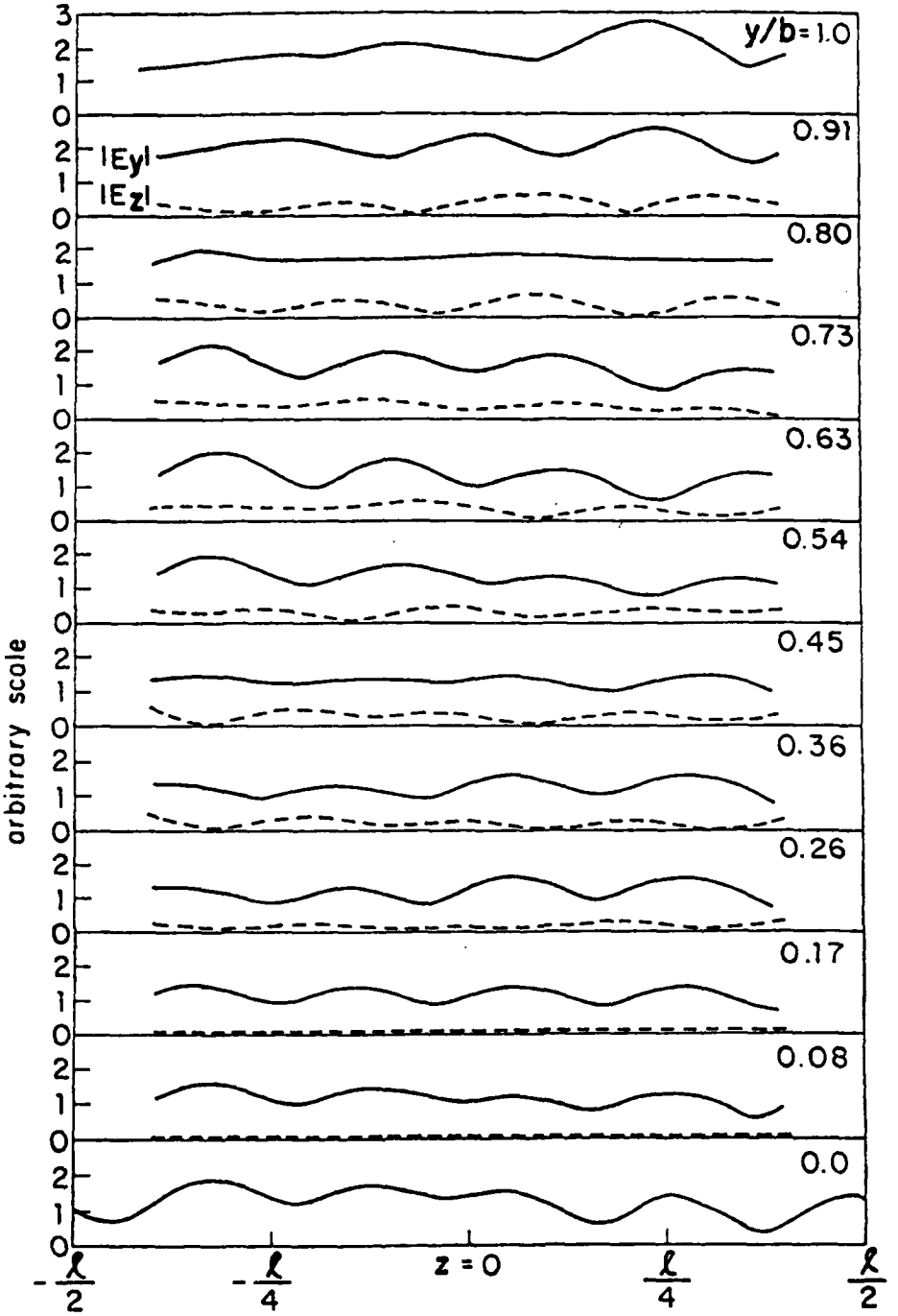

Longitudinal cross section of working volume y-z plane; x = 1.7 cm, ℓ = 115 cm = 2.4 λ, and b = 108 cm = 2.25 λ

Figure 11. Measured magnitude of the vertical and longitudinal components of the electric field in the working volume.

long tube parallel to the x-axis that moves laterally and vertically. The component E_y was measured with the dipole in the vertical position, the component E_z with the dipole in the horizontal position. Only the magnitudes $|E_y|$ and $|E_z|$ are shown in Figure 11. Actually, both magnitude and phase were measured. Furthermore, for each height y/b shown in Figure 11 except $y/b = 0$, the fields were measured at seven values of x covering one-half of the parallel plate region.

Extensive field measurements have been made at $y/b = 0.08$, 0.45, and 0.91 with the space probe and at $y/b = 1$ with the monopole probe protruding from the top plate. These measurements were reported in Wu, et al. (Ref. 22) and Krook, et al. (Ref. 23). Of particular interest are the four graphs of $|E_y|$ shown in Figure 12. They reveal the striking change in the standing-wave pattern in the plane $x = 1.7$ cm from near the top ($y/b = 0.91$) to the near bottom ($y/b = 0.079$). Clearly there are three standing-wave maxima at the top, and four at the bottom. Actually, the standing-wave pattern for $|E_y|$ at $y/b = 0.079$ near the ground plane and shown at the bottom in Figure 12 is a good approximation of the TEM field. The successive maxima are quite uniformly spaced at $\lambda/2 = 24$ cm and $E_z = 0$. On the other hand, the standing-wave pattern of $|E_y|$ at $y/b = 0.91$ near the top plate is quite different in that there are more nearly three instead of four standing half-wavelengths in the distance $-48 \text{ cm} \leq s \leq 48$ cm. This is shown at the top in Figure 12. It is also evident from Figure 11 that E_z is significant. It has a standing-wave distribution with a wavelength near λ_{g3} and is displaced from that of $|E_y|$ by nearly $\lambda_{g3}/4$.

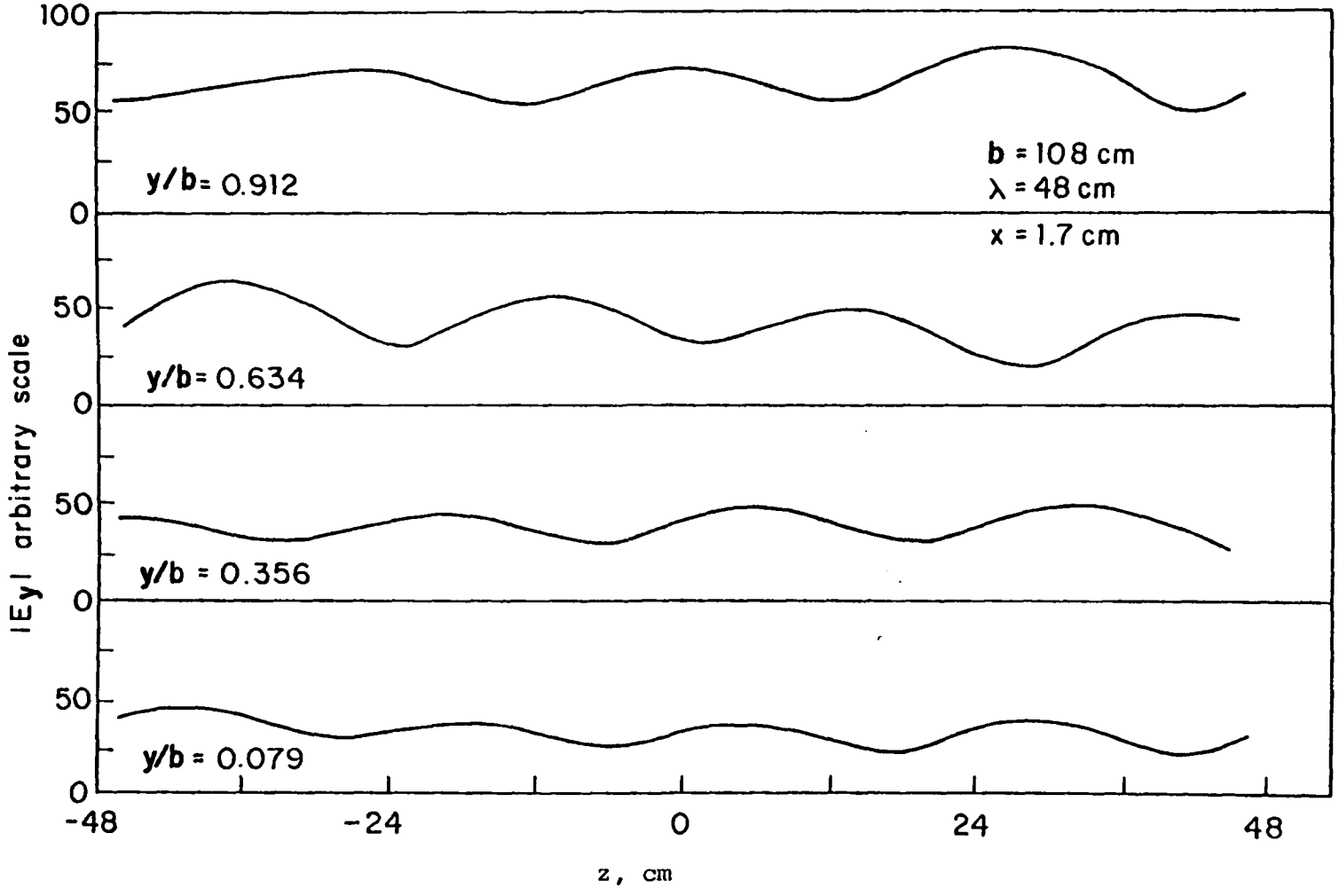

Figure 12. Measured $|E_y|$ near center (x = 1.7 cm) of working volume at four heights.

In order to interpret the extensive data contained in the measured field in the working volume, the graphs shown in Figure 13 were constructed from the measured data. They show the measured $|E_y|$ as a function of the vertical coordinate y at seven different transverse positions x across the central plane $(z = 0)$ of approximately one-half of the parallel plate region. The distributions are quite comparable in magnitude and shape, thus indicating a field that is reasonably independent of the transverse coordinate x, as is implicit for the ideal TEM and TM_{0n} components. The fact that E_y is approximately independent of x also indicates that the contribution to $|E_y|$ by possible $TE_{0\ell}$ modes is small.

At each cross section (z = constant), E_y can be approximated by a superposition of the TEM and the three propagating TM_{0n} modes. The relative amplitudes of these modes cannot be determined theoretically, but can be obtained from the measured distribution of E_y. This superposition of modes has been demonstrated in Figures 14a and 14b.

It is evident from these figures that the assumed approximate representation of the field as a superposition of the ideal parallel-plate TEM and TM_{0n} modes is a good one throughout the working volume of the model simulator. It is also evident that the total E_y differs greatly from the part contributed by the TEM mode alone, which is constant in y. Such a representation has also shown that the amplitudes of the TEM and TM_{01} modes are almost the same. Their standing-wave distributions and phases are such that $|E_y|$ is substantially greater near the top plate, $y = b$, than near the ground plane, $y = 0$.

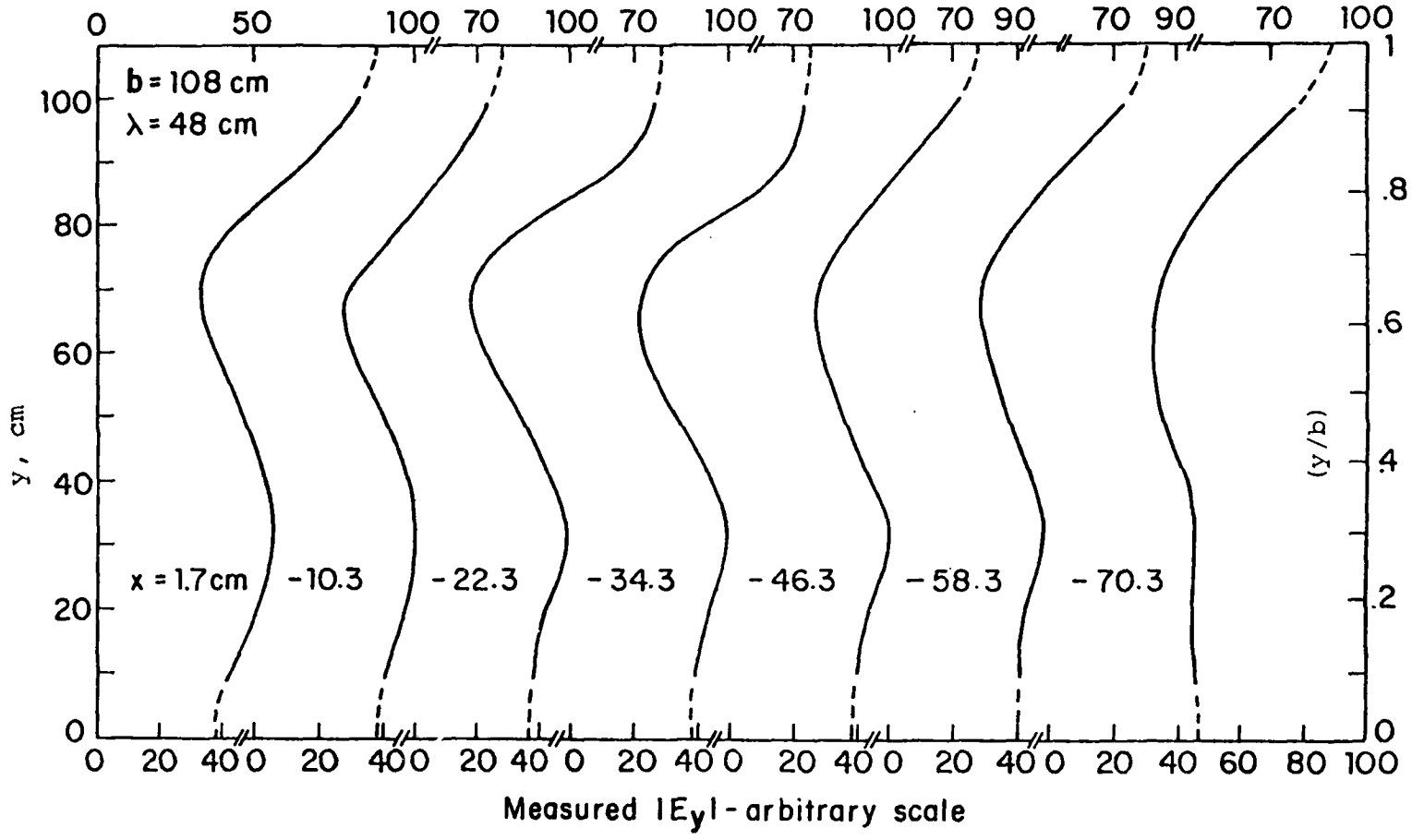

Figure 13. Measured electric field near central plane (z = 0) in parallel-plate region.

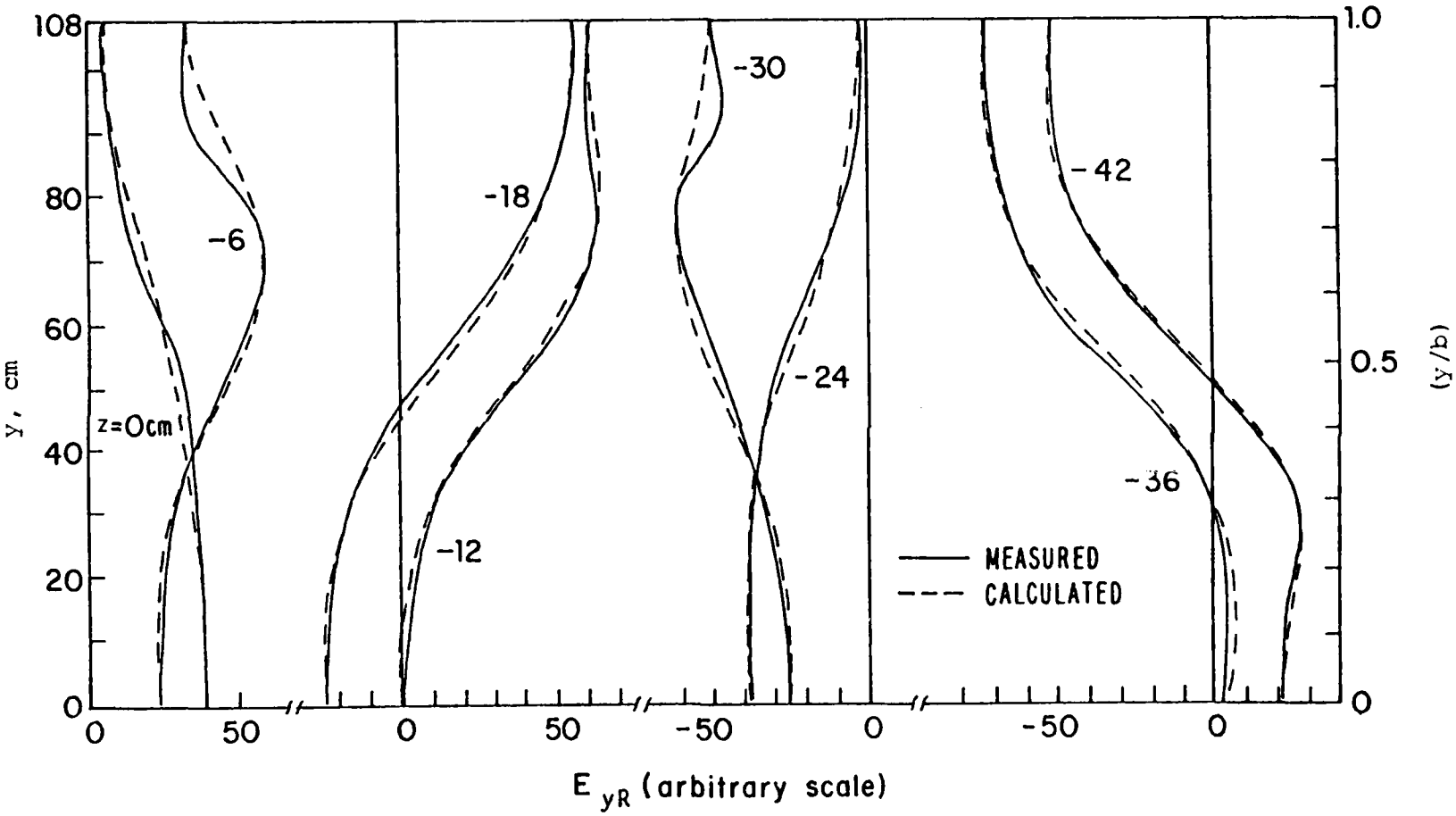

Figure 14a. Real part of vertical electric field in working volume. (Phase reference: x = y = z = 0).

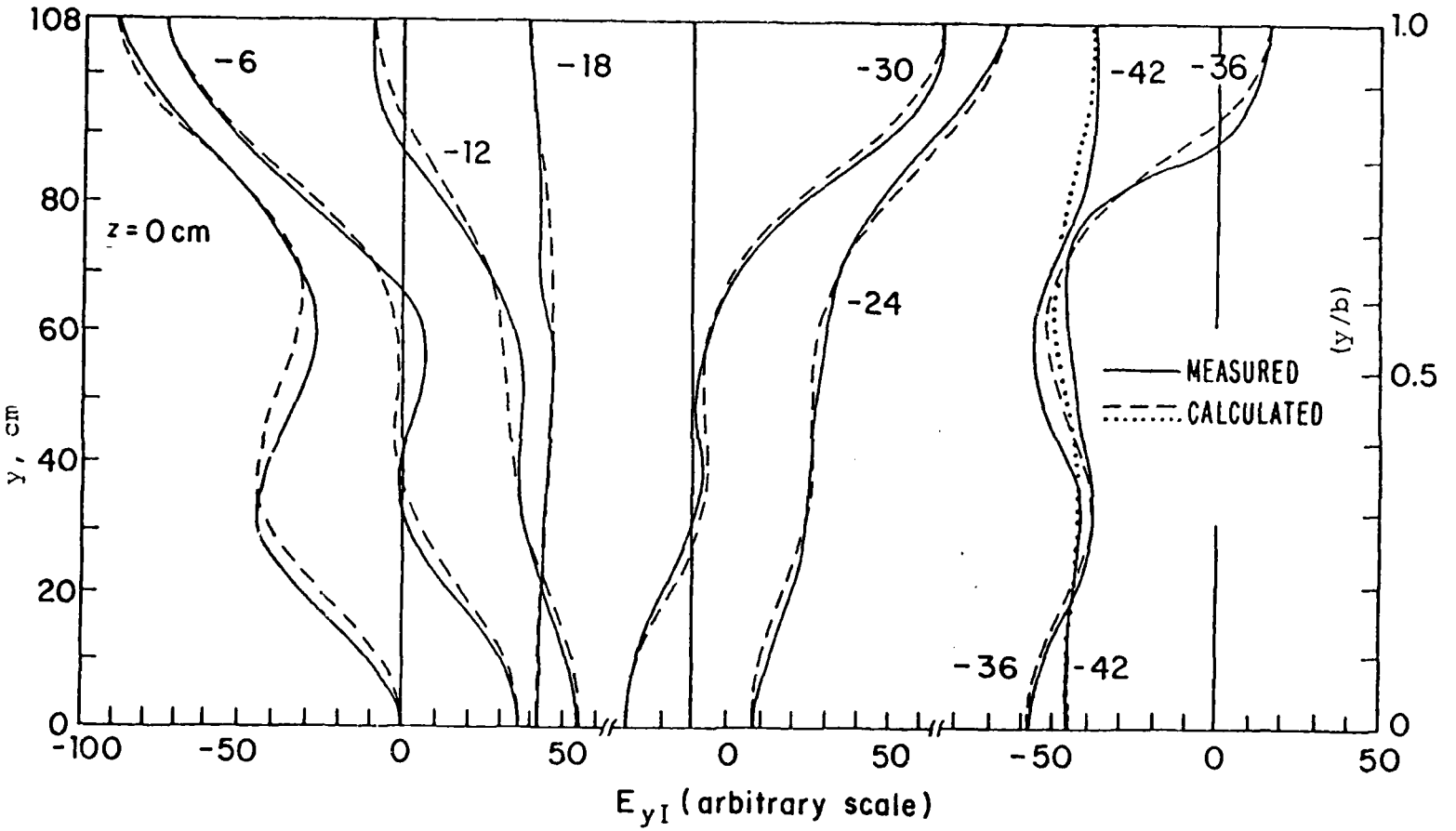

Figure 14b. Imaginary part of vertical electric field in working volume. (Phase reference: x = y = z = 0).

4. THE MEASURED FIELD IN THE WORKING VOLUME:

$b = 0.66\lambda = 75$ cm; $f = 264$ MHz

The components E_y and E_z in the working volume and adjacent regions were also measured with $f = 264$ MHz when $b = 75$ cm $= 0.66\lambda$ and $\lambda = 113.6$ cm. To simplify the presenstation of the data, these components of the field were measured as functions of y/b with $z = 0$ and x as parameters. The measured graphs of $|E_y|$, $|E_z|$, θ_y and θ_z are shown in Figure 15 for eight values of x.

As with the higher frequency and greater height b of the working volume, the approximate representation of E_y and E_z by the TEM and TM_{0n} modes was found to be quite satisfactory. The difference is that at $f = 626.5$ MHz, it took 3 TM modes, whereas at $f = 264$ MHz, it took only the TM_{01} mode in addition to the TEM mode for adequate representation of measured fields.

The approximate representation of the electric field in the parallel-plate region of the simulator in terms of the TEM and TM_{0n} modes tacitly assumes that all of the components of the electromagnetic field are independent of the transverse variable x, since all wavefronts are assumed to be planes perpendicular to the longitudinal Z-axis. This was taken to be a good approximation because the electricl field shown in Figure 13 changes relatively little as x is varied. By examining the variation of the field with the x-coordinate in great detail, it was basically concluded that the contributions made by the TE_{01} modes, if any, are negligible at both frequencies (626.5 MHz and 264 MHz) compared to the combined contributions of TEM and TM_{0n} modes. This conclusion was reached starting with the nature of the wavefronts on the surfaces of constant phase in the parallel plate region and recognizing this to be a traveling spherical wave with superimposed oscillations due to standing waves. The

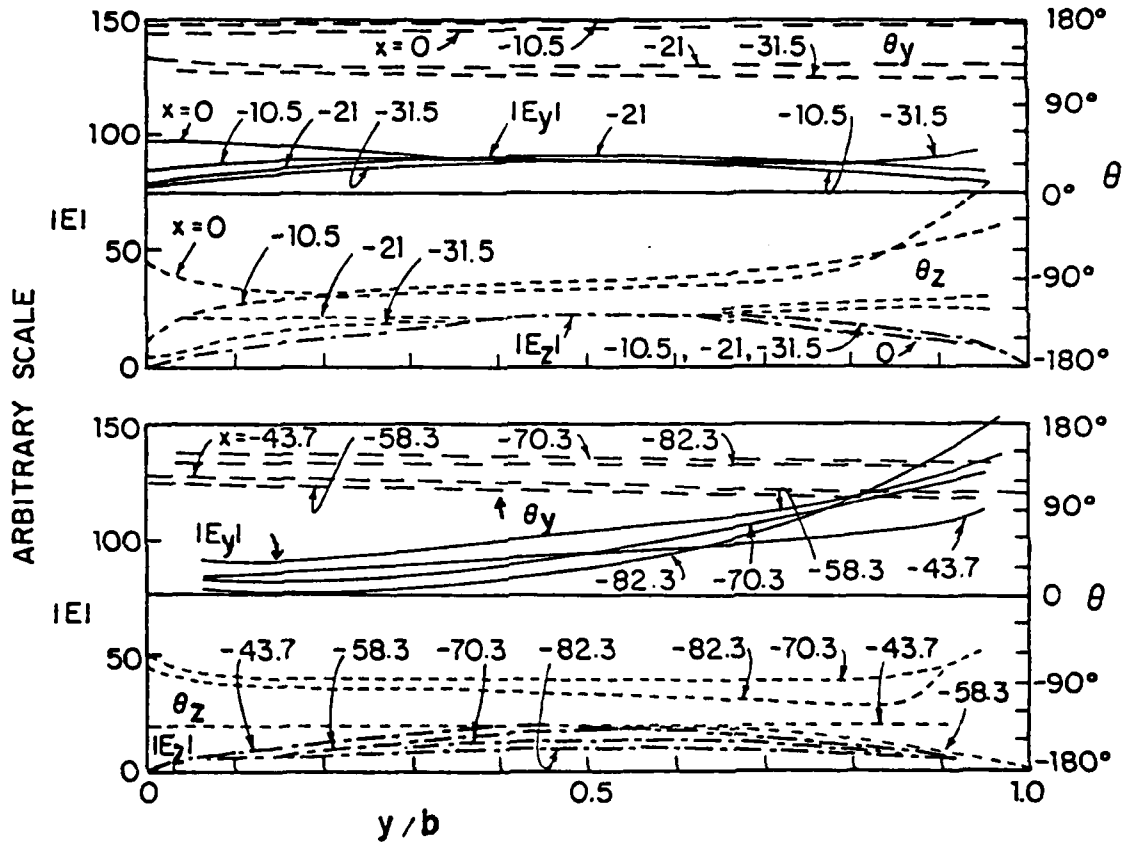

Figure 15. Measured electric field in transverse plane, z = 0, of parallel-plate region: ℓ = 114.8 cm, 2a = 175 cm, b = 75 cm, and f = 264 MHz.

incident spherical wave can excite antisymmetric components of H_z and can potentially excite antisymmetric $TE_{0\ell}$ modes. The amplitudes and wave members of $TE_{0\ell}$ modes are known for certain dimensions (Ref. 27). From examining the data, it is reasonable to suppose that a superposition of $TE_{0\ell}$ modes will account for the difference $E_y(x,y,z) - E_y(0,y,z)$ where $E_y(0,y,z)$ is the field represented by TEM and TM_{0n} modes, and to assume that the TE_{11} mode contributes negligibly. For this section, the representation of the electromagnetic field in terms of TEM and TM_{0n} modes is adequate without the addition of a sum of $TE_{0\ell}$ modes, because it has been experimentally verified that the departure of $E_y(x,y,z)$ from $E_y(0,y,z)$ is quite small--about 8%--in the central part of the simulator.

This completes the survey of the incident field at two frequencies (626.5 and 264 MHz) and their subsequent decomposition into TEM and TM_{01} modes. Before one attempts to suppress the undesirable TM_{0n} modes, a clear understanding of the incident field in terms of modes, as demonstrated in this section, is essential.

III. CHARACTERISTICS OF NON-TEM MODES

As was experimentally demonstrated in the preceding section, an open waveguide formed by two perfectly conducting parallel plates of finite width can support, in addition to the dominant TEM mode, higher-order TE and TM modes. These higher modes have suitably complex propagation constants which account for the radiation loss of the modes. Because of radiation, power flow and stored energy are not confined to the inner region of the structure. As the wave (a superposition of modal distributions) propagates, there is a continuous leaking of energy from the open waveguiding structure.

In closed waveguides, the higher modes are the solutions of source-free time harmonic Maxwell's equations characterized by axial field variation of the form $\exp [j(\omega t - zk_z)]$. Each one of these modes with real propagation constants (k_z) below cutoff satisfies all of the boundary conditions. Above cutoff k_z is pure imaginary and the modes are evanescent. Also, these modes possess finite energies in a cross section and display orthogonality and completeness properties.

In contrast, the modes on an open waveguide form a discrete spectrum of leaky modes satisfying Maxwell's equations and boundary conditions. However, any cross section extends to infinity and the fields can grow without bounds at large distances from the simulator cross section. These leaky modes on open waveguides do not form a complete orthogonal set and have to be supplemented by a continuous spectrum. The variation of an arbitrary mode can be separated into transverse and longitudinal parts as follows:

$$\tilde{F}(x,y,z,s) = \tilde{f}(x,y,s)\ e^{-\zeta z} \qquad (6)$$

where $\tilde{F}$ denotes an arbitrary field component, and $\tilde{f}$ denotes variation in the transverse (x-y) plane. The exponential factor displays axial (z coordinate) variation with ζ (Laplace transformation variable corresponding to the z coordinate) being the longitudinal complex wavenumber. The complex frequency is denoted by s, and it is the Laplace transformation variable corresponding to the time t. Setting,

$$p^2 = (s^2/c^2) - \zeta^2 = (\gamma^2 - \zeta^2) \tag{7}$$

gives,

$$\zeta = \pm\sqrt{\gamma^2 - p^2} \tag{8}$$

To exhibit the cutoff behavior, consider $s = j\omega$, $\gamma = jk$ and $\zeta = jk_z$

$$\zeta = jk_z = \pm\sqrt{(jk)^2 + (\pm jp)^2} = \pm j\sqrt{k^2 + p^2} \tag{9}$$

or, $$k_z = \pm\sqrt{k^2 + p^2} = (\beta + j\alpha) \tag{10}$$

In the integral equation formulation (Ref. 1), complex p, multiplied by a factor with linear dimension appears in the argument of special functions. In order to compute the various field quantities, one looks for the roots of transcendental complex functions of p in the complex p-plane. These functions are obtainable in closed form for the limiting cases of narrow and wide plates. Denoting a typical root by $p_{n,m}$, the corresponding longitudinal complex wavenumber for this arbitrary mode becomes

$$k_{z_{n,m}} = \pm\sqrt{k^2 + p_{n,m}^2} = \beta_{n,m} + j\,\alpha_{n,m} \tag{11}$$

$p_{n,m}$ values of interest are almost purely imaginary with relatively small negative real parts. Let

$$p_{n,m} = u_{n,m} + j\, v_{n,m} \quad ; \quad (|u_{n,m}| << |v_{n,m}|)$$

so that

$$k_{z_{n,m}} = \pm\sqrt{(k^2 + u_{n,m}^2 - v_{n,m}^2) + 2j\, u_{n,m}\, v_{n,m}} \qquad (12)$$

If $p_{n,m}$ was purely imaginary (i.e., $u_{n,m} = 0$), the cutoff behavior depends upon the value of the factor $\pm\sqrt{k^2 - v_{n,m}^2}$. Non-TEM modes do not propagate when $v_{n,m}^2$ exceeds k^2 which makes k_z purely negative imaginary

$$k_z \xrightarrow[v_{n,m}^2 > k^2]{} -j\,|k_z|$$

and the resulting argument of $\exp(-j\, k_z z)$ is negative real. The cutoff behavior for the special case when [$s=j\omega$, $\gamma=jk$ and $p_{n,m}=j\, v_{nm}$] can be summarized as follows. For these special conditions, the longitudinal wavenumber k_z is given by

$$k_{z_{n,m}} = \begin{cases} \beta_{n,m}; \text{ [with } \beta_{n,m} > 0 \text{ and } \alpha_{n,m} = 0\text{]} & \text{for propagation} \\ \beta_{n,m} + j\alpha_{n,m}; \text{ [with } \beta_{n,m} > 0 \text{ and } \alpha_{n,m} < 0\text{]} & \text{for evanescence} \end{cases} \qquad (13)$$

Correspondingly, the longitudinal variation of the fields $\exp(-j\, k_{z_{n,m}} z)$ exhibits the transition from propagation into evanescence. However, the complex singularities ($p_{n,m}$) do have small negative real parts, and the transition near cutoff is less abrupt. In the regime of evanescence, the longitudinal wavenumber $k_{z_{n,m}}$ becomes largely purely negative imaginary with a small real part. Consequently, the exponential longitudinal variation $\exp(-j\, k_{z_{n,m}} z)$ exhibits evanescence.

Furthermore, a waveguiding structure formed by two finitely wide plates has two planes (x=0 and y=0) about

which the fields can be symmetric or antisymmetric (Ref 28). Such symmetry decomposition can be represented symbolically by indexing the p-plane singularities as

$$p_{n,m}^{(\pm,\pm,E \text{ or } H)}$$

where n and m correspond to the field variations in the x and y directions. The two ± signs in the superscript indicate symmetry or antisymmetry along the transverse x and y directions, and E or H denote either the TM or TE mode. Thus, such a representation of the p-plane singularities uniquely specifies a mode and its symmetry properties. Consistent with the above notation, the modes themselves can be denoted by $E_{n,m}^{(\pm,\pm)}$ (or $TM_{n,m}^{(\pm,\pm)}$) and $H_{n,m}^{(\pm,\pm)}$ (or $TE_{n,m}^{(\pm,\pm)}$).

These modes in open waveguides formed by a pair of finitely wide parallel plates are found by formulating two different scalar integral equations (of the first kind) for the current and charge densities on the plate. Under certain approximations (separation >> width or vice versa), the integral equations can be solved analytically by first tranforming them into a Fredholm integral equation of the second kind (Refs. 1,4, and 5) and using perturbation techniques.

It is not our intention to show detailed modal distributions of these higher modes in this section but to point out the methods employed and availability of field plots. Specific calculations of the TM modes in a geometry corresponding to the model EMP simulator at Harvard are available if more accuracy is required for comparisons with the measured data. However, as was shown in the previous section, the modes of infinitely wide parallel plates are adequate for comparison with the measured data, leading to unambiguous identification of the various modes supported in the simulator.

IV. ELECTROMAGNETIC CONSIDERATIONS OF SPATIAL MODAL FILTERS

The object of introducing a spatial modal filter (SMF) is to load or damp the non-TEM modes (i.e., TE, TM) without significantly disturbing the TEM modes. One method that has been experimentally implemented in the context of TEM cells (Ref. 29) with some degree of success is by inserting radio frequency (RF)-absorbing material (Refs. 30 and 31) along the conducting walls of the waveguiding structure. This technique lacks an analytical basis and also does not fully exploit the uniform characteristics of the dominant TEM mode for damping the non-TEM modes. Hence, by recognizing the fact that all propagating modes have spatial properties, one can take advantage of certain spatial properties to selectively load the modes (Ref. 32). In a two-parallel-plate transmission-line type of EMP simulator, all of the important characteristics of the principal TEM mode, both in the parallel-plate region (Ref. 9) and the conical plate region (Refs. 10 and 11), are well known and documented. The quantities of interest are the characteristic impedance, equipotential and field distributions, and field uniformity. Later in this section knowledge of these quantities are used in developing a spatial modal filter. Such filters can take various forms and are dimensionally categorized in the following subsections.

1. ZERO-DIMENSIONAL SMF

A zero dimensional spatial modal filter acts essentially like a directional coupler in a transmission line that couples to backward propagating modes. In the case of a simulator under consideration, this type of SMF can take the form of two receiving or parasitic antennas (equivalent dipoles, loops) suitably oriented on the top plate or the ground plane so that the TEM mode is uncoupled. The sensitivity of damping of the non-TEM is governed by local field ratios.

2. ONE-DIMENSIONAL SMF

One-dimensional SMFs can be implemented by having longitudinal slots both in the top plate and the ground plane. The longitudinal slots (directed along the z-axis of Figure 1 in the parallel-plate region and directed along the spherical radial coordinate in the conical region) will be resistively loaded by transverse resistors (x-direction in Figure 1). By definition, the only mode with longitudinal component of magnetic field (H_z) is the TE mode and, hence, this mode has principally transverse currents (J_x) which couple to the transverse resistors. Consequently, this form of SMF is essentially uncoupled from the principal TEM or higher TM modes while loading the higher TE modes.

3. TWO-DIMENSIONAL SMF

An extension of the one-dimensional SMF is to introduce loading sheets that are comprised of a two-dimensional (transverse and longitudinal) array of resistors. In the top plate and the ground plane, one would have only transverse resistors, but in the space away from the simulator plates, the loading sheet will be two-dimensional. The sheet will be located along an equipotential surface of the principal TEM mode. This implies that the sheet is electromagnetically invisibile to the principal TEM mode while coupling and, hence, damping the non-TEM modes.

4. THREE-DIMENSIONAL SMF

The two-dimensional loading sheet described above can be repeated to fill some portion of the volume between the top plate and the ground plane resulting in a volumetric suppressor of non-TEM modes.

There are certain constraints to be placed on the choice of the volume of space wherein such a filter can be placed. For example, the filter should not be close to the working

volume of the simulator to avoid any coupling to the test object. Furthermore, the higher-order TE and TM modes become evanescent at a certain distance away from the terminator in the output section. For this reason, little is gained by placing the volumetric SMF near the termination. Such considerations indicate that the SMF should be placed under the output bend extending toward, but not close to, the terminator.

Section V develops two approximate analytical methods for estimating the sheet resistors.

V. ESTIMATION OF SHEET IMPEDANCES

This section derives relations useful in estimating sheet impedances of the SMF. Essentially, two approaches are taken as outlined below:

(1) Assuming that a two-dimensional arrangement can simulate a resistive sheet, an approximate analytical method, based on the incidence of non-TEM (TE and TM) modes, is developed. This method yields relations useful in estimating the longitudinal and transverse resistor values.

(2) By using a more rigorous method of mode matching at the appropriate interfaces, one can formulate a boundary value problem that leads to an optimization of the sheet impedance. In this formulation, the resistive sheet bifurcates and the incident wave is a propagating TM_{01} mode with the longitudinal electric field attaining a maximum in the middle of the waveguide. This provides maximum coupling to the resistive sheet.

1. APPROXIMATE METHOD

In this subsection, relations are derived that are useful in estimating the longitudinal and transverse resistor values in the individual sheets of a volumetric suppressor. A cross-sectional view of the SMF is sketched in Figure 16. Essentially the mode filter would consist of several layers of resistor arrangement, wherein each layer consists of a two-dimensional array of resistors along the axial and transverse directions. Each layer would coincide with a TEM equipotential surface in a conical transmission line. The equipotential and field calculations in a conical transmission line have been reported (Refs. 10 and 11) and they are based on stereographically projecting the two-conical-plate line into a cylindrical

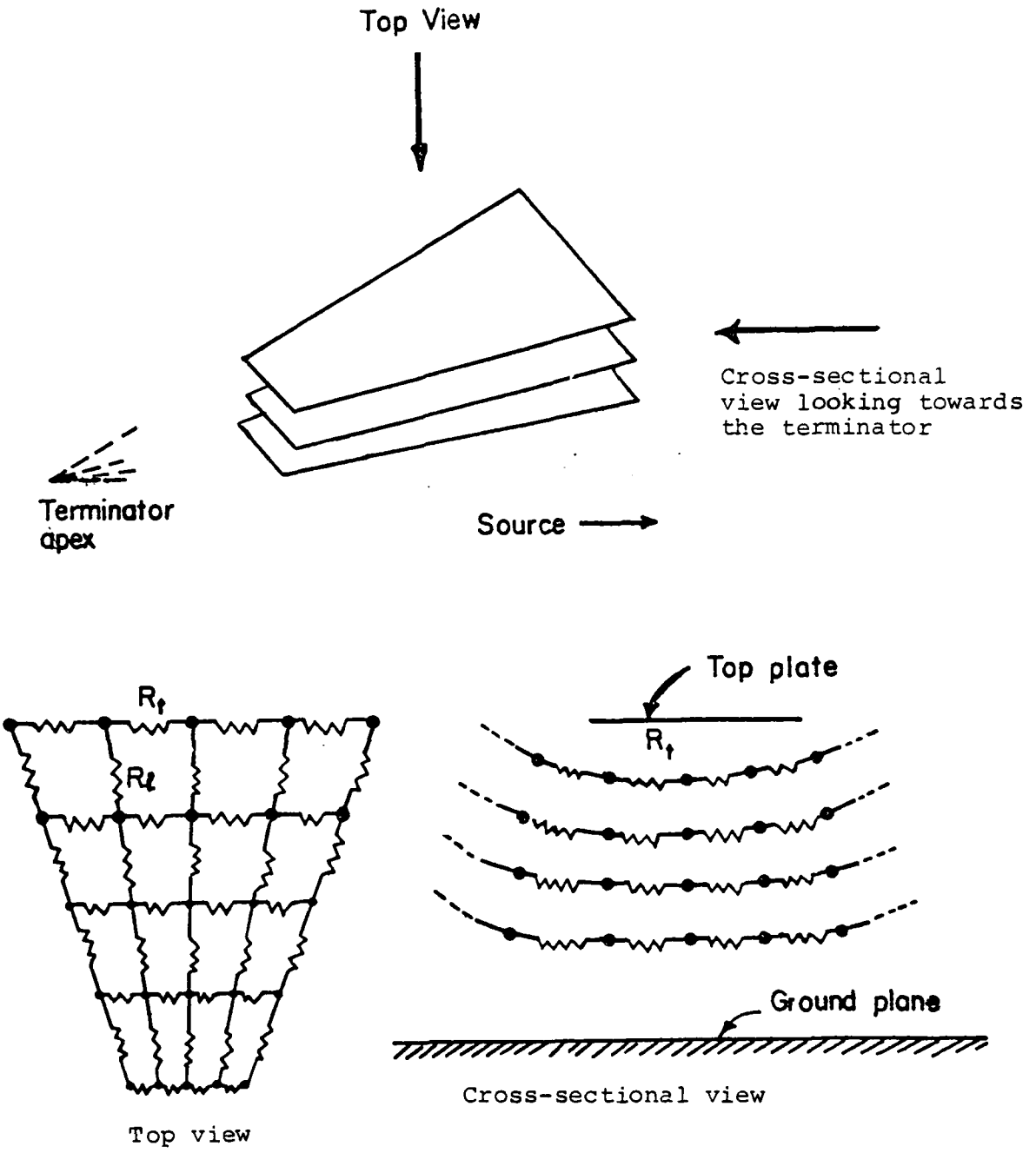

Figure 16. Structure of the volumetric spatial modal filter.

line of two circular arcs on two different circles. The curved-cylindrical-plate problem is later solved by conformal mapping of the TEM quantities. The physical quantity that is relevant for the SMF design is the TEM equipotential surface, an example of which is shown plotted in Figure 17. In this figure, the top plate is held at a potential of V_o with the ground plane as the reference. The equipotentials (magnetic field lines) are shown in steps of 0.1 V_o and the stream lines (electric field lines) in steps of 0.1 U_o. U_o is the total current flowing on half of the top plate. The individual resistive sheets of the volumetric suppressor will be made to coincide with the calculated surfaces.

In estimating the values of the transverse (R_t) and the longitudinal (R_ℓ) resistors, it is useful to view the two-dimensional array of resistors on any given equipotential surface as a resistive sheet with an impedance of Z_s. Now, consider the following two canonical problems useful in estimating R_ℓ and R_t. The two problems are posed and analyzed by viewing the mode suppressor sheets as plane wave absorbers.

a. TM Waves Incident on the Resistive Sheet

Consider a TM wave incident on the resistive sheet (Z_s in Ω), as shown in Figure 18(a). Denoting the induced surface current density on the sheet by J_s(A/m), the boundary conditions on the tangential components of the electric and magnetic field lead to

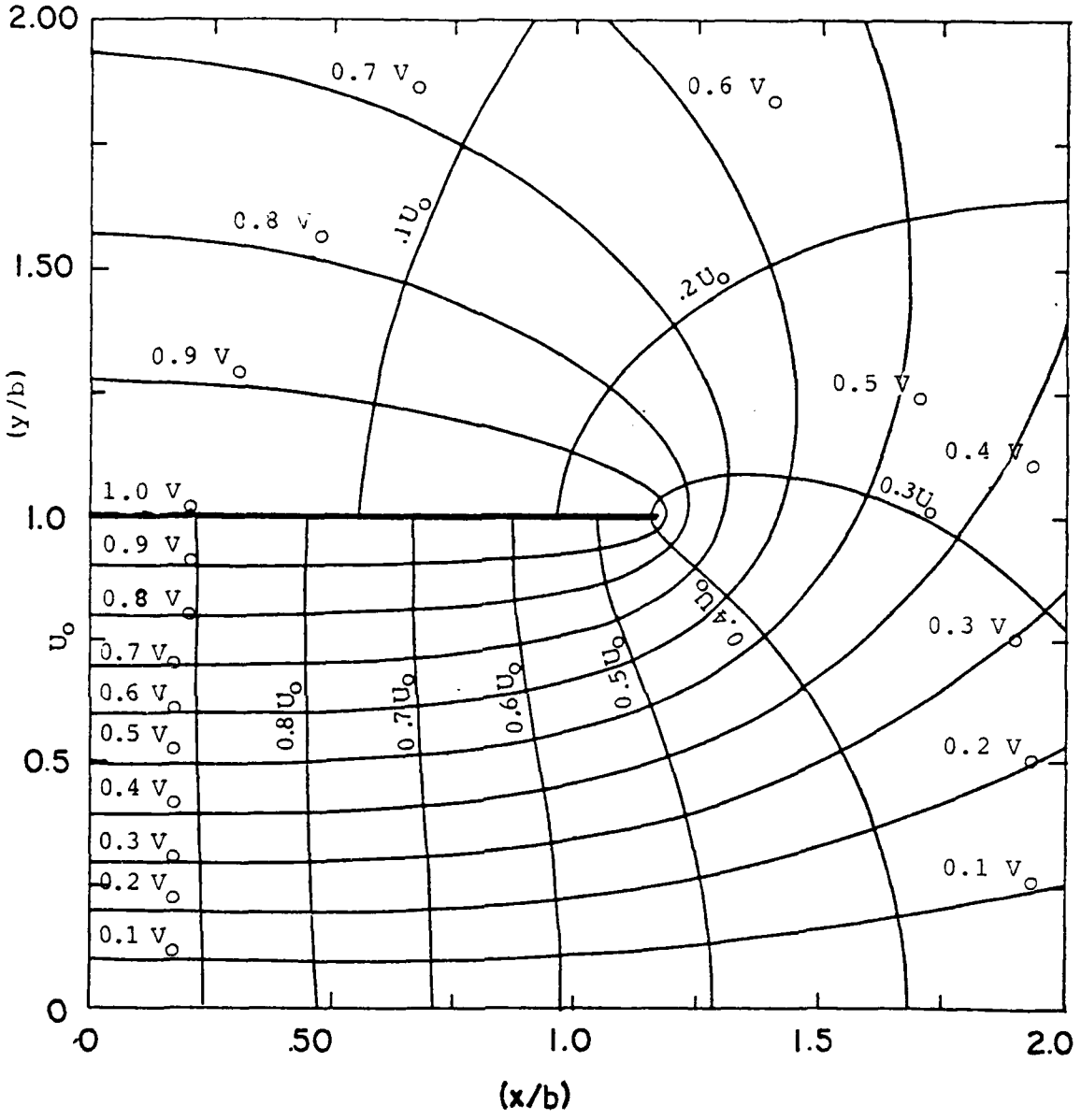

Figure 17. A typical TEM equipotential and electric field lines in the conical transmission line ((b/a) = 0.857 and (L/b) = 4.2; scale model simulator with $Z_c^{(TEM)}$ = 82 Ω from top plate to ground plane).

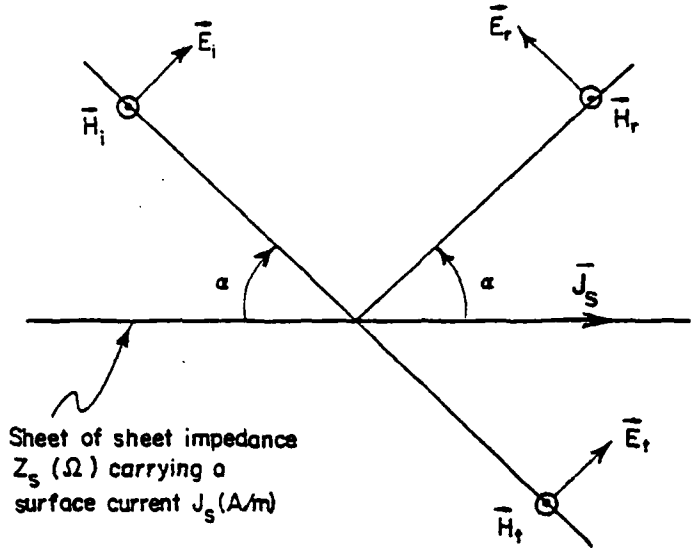

(a) TM wave incident on a resistive sheet

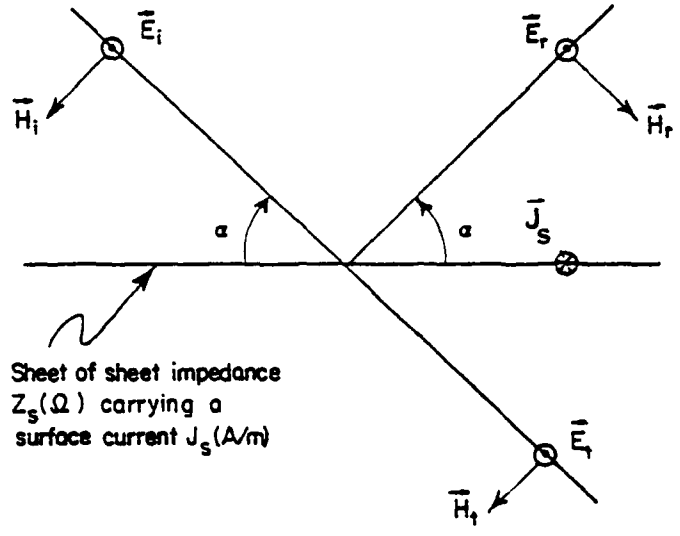

(b) TE wave incident on a resistive sheet

Figure 18. Mode suppressor viewed as plane wave absorbers.

$$E_{tan} = E_i \sin(\alpha) - E_r \sin(\alpha) = E_t \sin(\alpha) \tag{14}$$

The difference in the tangential magnetic field is

$$\Delta H_{tan} = H_{top} - H_{bottom} = H_i + H_r - H_t = J_s = E_{tan}/Z_s \tag{15}$$

J_s is positive and is directed from left to right in Figure 18a. Note that the free space characteristic impedance Z_o is given approximately by

$$Z_o = \frac{E_i}{H_i} = \frac{E_r}{H_r} = \frac{E_t}{H_t} \simeq \sqrt{\frac{\mu_o}{\epsilon_o}} \tag{16}$$

Using Equation (16) in Equation (15), along with $E_r = E_i - E_t$ from Equation (14), gives

$$\frac{E_t}{E_i} = \frac{2 Z_s}{2 Z_s + Z_o \sin(\alpha)} \tag{17}$$

For fixed values of E_i and α, the power dissipated in the sheet per unit area,

$$P = E_{tan} J_s = (E_{tan}^2/Z_s) = (E_t^2 \sin^2(\alpha)/Z_s)$$

$$= \frac{E_i^2 \sin^2(\alpha)}{Z_s} \left(\frac{2 Z_s}{2 Z_s + Z_o \sin(\alpha)} \right)^2 \tag{18}$$

Now the power dissipated as heat from the incident wave per unit area normal to the incident wave is

$$P_W = P/\sin(\alpha) = \left(\frac{E_i^2}{Z_o} f\right) \tag{19}$$

where f is the fractional power lost, and is given by

$$f = \frac{Z_o}{E_i^2} \frac{P}{\sin(\alpha)} = \frac{Z_o}{Z_s} \sin(\alpha) \left(\frac{2 Z_s}{2 Z_s + Z_o \sin(\alpha)}\right)^2 \tag{20}$$

Setting

$$\eta = \frac{Z_s}{Z_o \sin(\alpha)} \tag{21}$$

gives

$$f = \frac{1}{\eta}\left[\frac{2\eta}{1 + 2\eta}\right] \tag{22}$$

The fractional power lost can now be maximized by requiring

$$\frac{df}{d\eta} = 0 \quad ; \quad \text{leading to} \quad \eta_{opt} = 1/2$$

This gives an optimum value for the sheet impedance of

$$Z_s^{(opt)} = \frac{Z_o \sin(\alpha)}{2} \tag{23}$$

Equation (23) is now useful in estimating the longitudinal resistors R_ℓ which carry the current for the TM mode of propagation.

b. TE Waves Incident on the Resistive Sheet

An entirely similar analysis as was used in the TM case can be used for the TE case. Consider a TE wave incident on a resistive sheet of impedance Z_s in Ω at an angle α as shown in Figure 18b. Let the induced surface current on the resistive sheet be denoted by J_s(A/m). The boundary conditions on the tangential fields are

$$E_{tan} = -E_i - E_r = -E_t \tag{24}$$

The difference in the tangential magnetic field is

$$\Delta H_{tan} = H_{top} - H_{bottom} = -H_i \sin(\alpha) + H_r \sin(\alpha) + H_t \sin(\alpha)$$

$$= J_s = (E_{tan}/Z_s) \tag{25}$$

J_s is positive and directed into the plane of the paper in Figure 18b. As before, using Equation (16) in Equation (25) and later using Equation (24), gives

$$\frac{E_t}{E_i} = \frac{2 Z_s \sin(\alpha)}{2 Z_s \sin(\alpha) + Z_o} \tag{26}$$

Once again, the power dissipated in the sheet per unit area is

$$P = E_{tan} J_s = (E_{tan}^2/Z_s) = (E_t^2/Z_s)$$

$$= \frac{E_i^2}{Z_s} \left(\frac{2 Z_s \sin(\alpha)}{2 Z_s \sin(\alpha) + Z_o} \right)^2 \tag{27}$$

Using Equation (19), the fractional power lost is now given by

$$f = \frac{Z_o}{E_i^2} \frac{P}{\sin(\alpha)} = \frac{Z_o}{Z_s \sin(\alpha)} \left(\frac{2 Z_s \sin(\alpha)}{2 Z_s \sin(\alpha) + Z_o} \right)^2 \qquad (28)$$

$$= \frac{1}{\nu} \left[\frac{2\nu}{1 + 2\nu} \right] \qquad (29)$$

where $\nu = (Z_s \sin(\alpha)/Z_o)$. Now the dissipated power may be maximized by requiring

$$\frac{df}{d\nu} = 0 \quad ; \quad \text{leading to} \quad \nu_{opt} = 1/2 \qquad (30)$$

This gives an optimum value for the sheet impedance of

$$Z_s^{(opt)} \simeq \frac{Z_o}{2 \sin(\alpha)} \qquad (31)$$

Once again, note that for the TE case, only the transverse resistors carry current and, hence, Equation (31) applies to the transverse resistors R_t.

In either case of TM or TE waves incident on the resistive sheets, the values of the resistors R_ℓ and R_t are dependent on the angle of incidence of these waves onto the sheets. In a simulator configuration, this angle (α) is, of course, a variable quantity and, consequently, an experimental optimization of the particular values of the resistors is inevitable.

However, at high frequencies, where ray-optic considerations apply, one can estimate the angle α by considering a typical ray path. It is estimated that the present high frequency ripple of ±30% can be reduced to within ±10%. At intermediate frequencies, the angles are harder to estimate, but effective removal of energy from the non-TEM modes results from multiple passes. It is likely that for E modes (TM case), the ratio of E_z to E_x or E_y may define an effective angle α.

For the experimental evaluation, initially, a typical angle may be chosen in designing the filter and, later, experimentation around these values will determine the final values.

In successfully implementing these concepts in a given experimental situation, there will be several associated problems and considerations unique to the experiment. For instance, in a model simulator experiment, the power levels are low and, hence, energy dissipation in the resistors is not a serious consideration. However, on a full-scale facility (e.g., ALECS), it may become necessary to place the resistors in plastic tubes filled with oil. Also, in an on-site configuration the mechanical problems of supporting and holding the sheet along equipotential contours are much more severe. There are questions like how far outward in the cross-section should the sheets extend. Such considerations and a detailed design, fabrication and evaluation of the proposed volumetric suppressor will form the subject of Section VI.

2. A MORE RIGOROUS METHOD

This subsection formulates the problem of a resistive sheet of $R\ \Omega$ per square bifurcating an infinitely wide parallel-plate waveguide as shown in Figure 19. The two parallel plates are infinitely wide along the x direction and, are separated by a finite distance $2b$ in the y direction, with the incident wave propagating along the $+z$ direction. A resistive sheet of $R\ \Omega$ per square is placed in the middle and it has a width of $2w$ along the wave propagating direction and is also of infinite extent in the transverse x direction. The cross-sectional views of the problem geometry are also shown in Figure 19. The objective of the problem is to find a value of R given the following parameters,

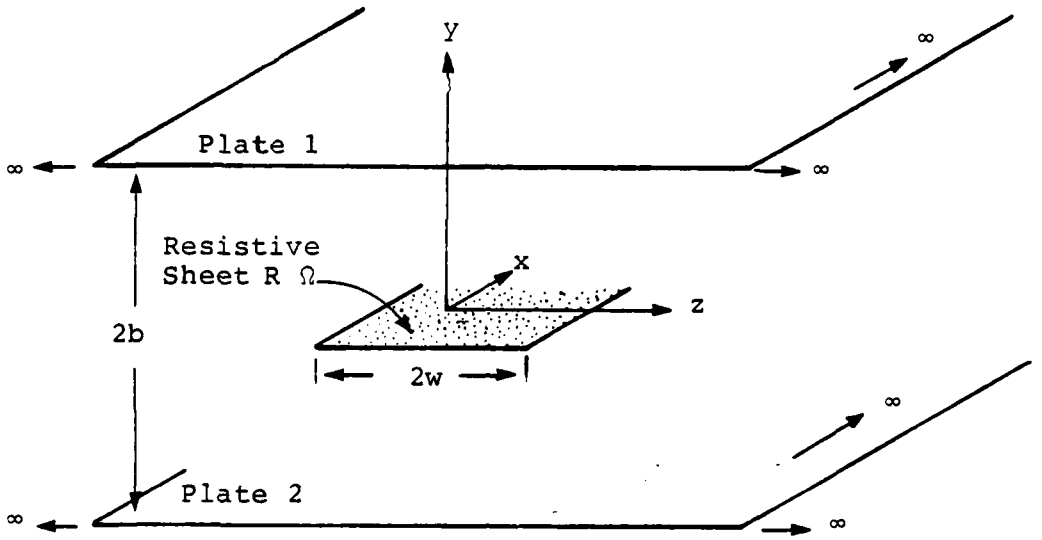

(a) Problem Geometry

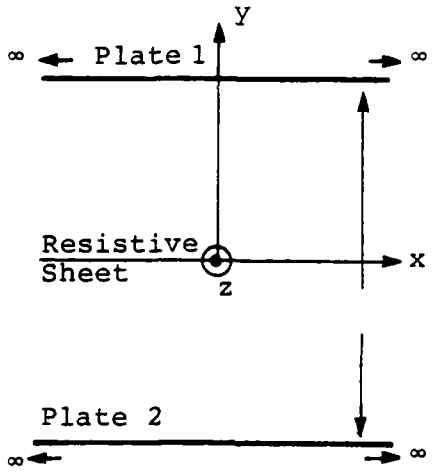

(b) xy plane

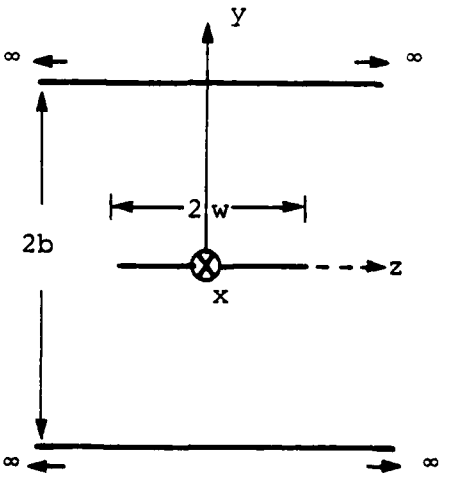

(c) yz plane

Figure 19. The problem of a resistive sheet bifurcating an infinitely wide parallel-plate waveguide.

that results in a maximum absorption of the incident wave and possibly a maximum absorption of the axial electric field of the TM mode.

R ≡ Value of the resistive sheet Ω per square
ω ≡ Radian frequency = $2\pi f$
ε_0 ≡ Permitivity of free space
b ≡ Half separation between plates
w ≡ Half width of the resistive sheet

In Figure 20a, a division of the region of interest into 3 parts is shown to facilitate the formulation. In region I, one essentially has an incident and reflected wave propagating respectively in the + and - z directions. In region II also, there could be + and - z propagating waves, whereas, in region III, the transmitted wave is the only propagating wave in the + z direction. Also, as may be seen in Figures 20b and 20c, the incident wave of interest is the symmetric TM mode with its axial (z directed) electric field having a maximum in the middle for effective coupling to the resisitve sheet. The antisymmetric TM mode has an axial electric field vanishing in the middle and hence will not couple to the resistive sheet.

Next, write down the fields in the various regions.

Region I

a) incident field

$$H_{xi}(y,z) = \sum_{n=1}^{\infty,2} C_{1n} \sin\left(\frac{n\pi y}{2b}\right) e^{-j\beta_n z} \tag{32}$$

$$E_{yi}(y,z) = \sum_{n=1}^{\infty,2} C_{1n} \left(\frac{\beta_n}{\omega\varepsilon}\right) \sin\left(\frac{n\pi y}{2b}\right) e^{-j\beta_n z} \tag{33}$$

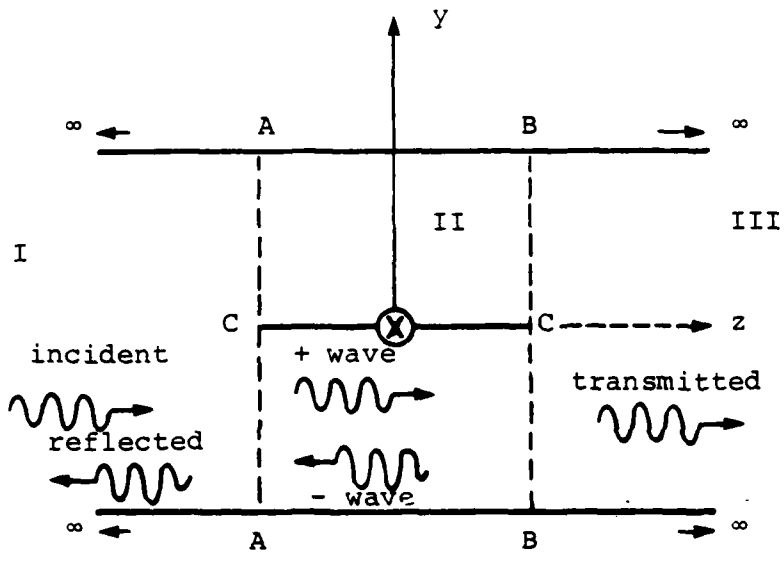

(a) Division into three regions

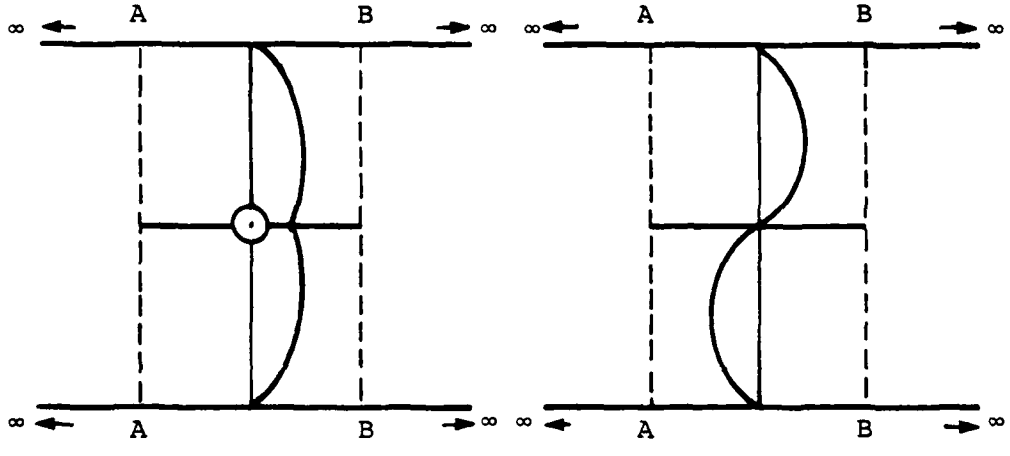

(b) Symmetric Case

(c) Anti-symmetric Case

Figure 20. Fields in various regions and two possible incident field configurations.

$$E_{zi}(y,z) = \sum_{n=1}^{\infty,2} C_{1n} \left(\frac{jn\pi}{\omega\varepsilon 2b}\right) \cos\left(\frac{n\pi y}{2b}\right) e^{-j\beta_n z} \tag{34}$$

b) reflected wave

$$H_{xr}(y,z) = \sum_{n=1}^{\infty,2} C_{2n} \sin\left(\frac{n\pi y}{2b}\right) e^{+j\beta_n z} \tag{35}$$

$$E_{yr}(y,z) = \sum_{n=1}^{\infty,2} C_{2n} \left(\frac{\beta_n}{\omega\varepsilon}\right) \sin\left(\frac{n\pi y}{2b}\right) e^{+j\beta_n z} \tag{36}$$

$$E_{zr}(y,z) = \sum_{n=1}^{\infty,2} C_{2n} \left(\frac{jn\pi}{\omega\varepsilon 2b}\right) \cos\left(\frac{n\pi y}{2b}\right) e^{+j\beta_n z} \tag{37}$$

where

$$\beta_n = \sqrt{\frac{\omega^2}{c^2} - \left(\frac{n\pi}{2b}\right)^2} \tag{38}$$

Note that, as required, in the incident field

$$H_{xi}(0,z) = E_{yi}(0,z) = E_{zi}(\pm b,z) = 0 \tag{39}$$

$$E_{zi}(0,z) = \sum_{n=1}^{\infty,2} C_{1n} \left(\frac{jn\pi}{\omega\varepsilon 2b}\right) e^{-j\beta_n z} \tag{40}$$

and similarly in the reflected wave

$$H_{xr}(0,z) = E_{yr}(0,z) = E_{zr}(\pm b,z) = 0 \tag{41}$$

$$E_{zr}(0,z) = \sum_{n=1}^{\infty,2} C_{2n} \left(\frac{jn\pi}{\omega\varepsilon 2b}\right) e^{+j\beta_n z} \tag{42}$$

Equation (40) ensures maximum coupling of the incident wave to the resistive sheet.

Region II

As was indicated earlier, there are two propagating waves in the + and - z directions in region II resulting in a standing wave distribution. It is immediately recognized that, because of the resistive sheet, the tangential electric field $E_z^{(+)}(0,z)$ and $E_z^{(-)}(0,z)$ do not vanish. The superscripts (+) and (-) refer to the positive and negative going waves respectively.

The field components for the + z directed wave are:

$$H_x^{(+)}(y,z)$$

$$= \left\{ \sum_{n=1}^{\infty,2} C_{3n}^{(s)} \left[\sin\left\{ \frac{n\pi}{2} \frac{(2y+b-\Delta_n)}{(b+\Delta_n)} \right\} \Big|_{-b}^{0} + \sin\left\{ \frac{n\pi}{2} \frac{(2y-b+\Delta_n)}{(b+\Delta_n)} \right\} \Big|_{0}^{b} \right] \right.$$

$$\left. + \sum_{n=1}^{\infty,2} C_{3n}^{(a)} \left[\sin\left\{ \frac{n\pi}{2} \frac{(2y+b)}{b} \right\} \Big|_{-b}^{0} - \sin\left\{ \frac{n\pi}{2} \frac{(2y-b)}{b} \right\} \Big|_{0}^{b} \right] \right\}$$

$$x \exp(-j\beta_n' z) \exp[-\alpha_n (z+w) \tag{43}$$

$$E_y^{(+)}(y,z)$$

$$= \left\{ \sum_{n=1}^{\infty,2} \left(\frac{\beta_n'}{\omega\varepsilon} \right) C_{3n}^{(s)} \left[\sin\left\{ \frac{n\pi}{2} \frac{(2y+b-\Delta_n)}{(b+\Delta_n)} \right\} \Big|_{-b}^{0} + \sin\left\{ \frac{n\pi}{2} \frac{(2y-b+\Delta_n)}{(b+\Delta_n)} \right\} \Big|_{0}^{b} \right] \right.$$

$$\left. \sum_{n=1}^{\infty,2} \frac{\beta_n'}{\omega\varepsilon} C_{3n}^{(s)} \left[\sin\left\{ \frac{n\pi}{2} \frac{(2y+b)}{b} \right\} \Big|_{-b}^{0} + \sin\left\{ \frac{n\pi}{2} \frac{(2y-b)}{b} \right\} \Big|_{0}^{b} \right] \right\}$$

$$x \exp(-j\beta_n' z) \exp[-\alpha_n (z+w)] \tag{44}$$

$$E_z^{(+)}(y,z)$$

$$= \left\{ \sum_{n=1}^{\infty,2} \frac{jn\pi}{\omega\varepsilon 2(b+\Delta_n)} C_{3n}^{(s)} \left[\cos\left\{ \frac{n\pi}{2} \frac{(2y+b-\Delta_n)}{(b+\Delta_n)} \right\} \Big|_{-b}^{0} + \cos\left\{ \frac{n\pi}{2} \frac{(2y-b+\Delta_n)}{(b+\Delta_n)} \right\} \Big|_{0}^{b} \right] \right.$$

$$\left. + \sum_{n=1}^{\infty,2} \frac{jn\pi}{\omega\varepsilon 2b} C_{3n}^{(a)} \left[\cos\left\{ \frac{n\pi}{2} \frac{(2y+b)}{b} \right\} \Big|_{-b}^{0} - \cos\left\{ \frac{n\pi}{2} \frac{(2y-b)}{b} \right\} \Big|_{0}^{b} \right] \right\}$$

$$x \exp(-j\beta_n' z) \exp[-\alpha_n (z+w)] \qquad (45)$$

In the above three expressions, the superscripts (a) and (s) refer to the antisymmetric and symmetric components respectively. Also, the delineation of terms by a vertical line at the end indicates the range of validity, e.g.,

$\Big|_{-b}^{0}$ - indicates that the particular term is applicable

in the bottom half of the waveguide for all x and for $|z| \leq w$, $-b \leq y \leq 0$.

The field components for the -z directed wave can be written down similarly, by essentially replacing C_{3n} and z by C_{4n} and -z. Also required are that the following boundary conditions at y=0 and y=±b be satisfied.

(a) tangential electric field vanishing on both plates

$$E_z^{(+)}(\pm b, z) = E_z^{(-)}(\pm b, z) = 0 \qquad (46)$$

(b) *continuity* of tangential electric field

$$E_z^{(+)}(0^+, z) = E_z^{(+)}(0^-, z) \qquad (47a)$$

$$E_z^{(-)}(0^+, z) = E_z^{(-)}(0^-, z) \qquad (47b)$$

(c) tangential magnetic field differing by true surface current

$$H_x^{(+)}(0^+, z) = - H_x^{(+)}(0^-, z) \neq 0 \tag{48a}$$

$$H_x^{(-)}(0^+, z) = - H_x^{(-)}(0^-, z) \neq 0 \tag{48b}$$

(d) For each n = 1,3,5 ..., and for both (+) and (-) waves, the boundary condition to be satisfied on the resistive sheet is

$$\left[\frac{E_z(0^+, z)}{H_x(0^-, z) - H_x(0^+, z)} \right] = R \tag{49}$$

When all of the appropriate field components are substituted into Equation (49), it results in the following transcendental equation for the complex number Δ_n

$$\frac{jn\pi}{\omega\varepsilon 4b(\delta_n+1)} \text{ cotan } \left\{ \frac{n\pi}{2} \frac{\Delta_n - b}{\Delta_n + b} \right\} = R \tag{50}$$

$$\frac{jn\pi}{\omega\varepsilon 4b(\delta_n+1)} \text{ cotan } \left\{ \frac{n\pi}{2} \frac{\delta_n - 1}{\delta_n + 1} \right\} = R \tag{51}$$

with the normalization

$$\delta_n = \Delta_n / b \tag{52}$$

Equation (51) can be solved in a straightforward manner for the complex parameter δ_n. One possible method is to write Equation (51) as $F(\delta_n) = 0$ by moving the term R to the left side and then looking for the zeros in the complex δ_n plane in a region where $F(\delta_n)$ is analytic, by making use of the computer programs developed in Reference (33). Next, the attenuation constant α_n for the TM_{0n} th mode has to be determined. At least for the cases of moderate losses, the following definition of α_n yields

$$\alpha_n = \left|\frac{\text{Power lost/unit length}}{2 \times \text{Power transmitted}}\right| \tag{53}$$

$$= \left|\frac{(1/2)\ H_x^2\ R}{(1/2)\ E_y\ H_x}\right| = \frac{R}{2(\beta_n'/\omega\varepsilon)}$$

$$= \frac{R\omega\varepsilon}{\sqrt{\frac{\omega^2}{c^2} - \left[\frac{n\pi}{2b}\left|\frac{\delta_n - 1}{\delta_n + 1}\right|\right]^2}} \tag{54}$$

Consequently, once the transcendental equation for δ_n is solved, it can be used in Equation (54) to determine the attenuation.

The electromagnetic field components in region III in terms of the transmitted wave can be written down as follows:

Region III

$$H_{xt}(y,z) = \sum_{n=1}^{\infty,2} C_{5n} \sin\left(\frac{n\pi y}{2b}\right) e^{-j\beta_n z} \tag{55}$$

$$E_{yt}(y,z) = \sum_{n=1}^{\infty,2} C_{5n}\left(\frac{\beta_n}{\omega\varepsilon}\right) \sin\left(\frac{n\pi y}{2b}\right) e^{-j\beta_n z} \tag{56}$$

$$E_{zt}(y,z) = \sum_{n=1}^{\infty,2} C_{5n}\left(\frac{jn\pi}{\omega\varepsilon 2b}\right) \sin\left(\frac{n\pi y}{2b}\right) e^{-j\beta_n z} \tag{57}$$

The remainder of the procedure will consist of the following steps. The unknown quantities at this stage are:

C_{1n}, C_{2n}, $C_{3n}^{(a)}$, $C_{4n}^{(s)}$, and C_{5n}. The desired quantities

E_{zr}/E_{zi} and E_{zt}/E_{zi}, which are indicative of the transmission of the TM_{0n} modes. By implication, they also indicate how well the resistive sheet can absorb the axial electric field incident on it. The unknown coefficients can be obtained by the method of mode matching at the two interfaces AA and BB. The continuity of fields across these interfaces require

$$\left.\begin{aligned} H_{xi} + H_{xr} &= H_x^{(+)} + H_x^{(-)} \\ E_{yi} + E_{yr} &= E_y^{(+)} + E_y^{(-)} \\ E_{zi} + E_{zr} &= E_z^{(+)} + E_z^{(-)} \end{aligned}\right\} \quad \text{at interface AA} \qquad (58)$$

$$\left.\begin{aligned} H_x^+ + H_x^- &= H_{xt} \\ E_y^+ + E_y^- &= E_{yt} \\ E_z^+ + E_z^- &= E_{zt} \end{aligned}\right\} \quad \text{at interface BB} \qquad (59)$$

recalling that the two interfaces are defined by

interface AA: $|y| \leq b$; $z = -w$, for all x
interface BB: $|y| \leq b$; $z = w$, for all x.

This formally completes the formulation and gives the option of determining the sheet resistors either using the approximate method of Section V-1 above or the more rigorous formulation of Section V-2. Because this concept of mode suppression has more experimental potential than analytical,

the approximate method was chosen in getting an initial value for the sheet impedance and then experimentally optimize the resistance value. In view of this, Section VI uses the formulas developed under the approximate method developed here and computes the initial resistor values.

VI. DESIGN AND METHODS OF EVALUATING A SPATIAL MODAL FILTER

Figure 21 illustrates the geometry of a parallel-plate transmission-line type of EMP simulator. Both the model simulator and ALECS structures have two planes of symmetry (x=0 and y=0). The half-separation and half-width of the plates are denoted by b and a and the horizontal length of the input or output conical regions by L. All of these parameters, along with the cone angle θ and the characteristic impedance $Z_c^{(TEM)}$ of the principal TEM mode, are given in Table 1 for both structures. Values of $Z_c^{(TEM)}$ are for the structure above the ground plane. They are interpolated from the values in Table 4.1 of Reference (9) which lists the impedance from plate to plate. It is seen from Table 1 that, although the model simulator is not an accurate scale model of ALECS, they are electromagnetically very similar. A basic difference in the two structures is in the construction of the top plate and the ground plane. In ALECS, the plates are made up of wire grids, whereas solid aluminum sheets are used in fabricating the model simulator. This difference, however, has a negligible effect on both the design and performance of the modal filter.

1. Resistive Sheet

The principal component of the electric field in the TEM mode is the normal component directed from the ground plane to the top plate. So, if one places resistors on a TEM equipotential surface along the axial and transverse directions, such a 2-dimensional array will have minimal effect on the TEM mode. However, for the TE modes (H modes), the transverse electric field couples to the transverse resistors and, in the case of the TM modes (E modes),

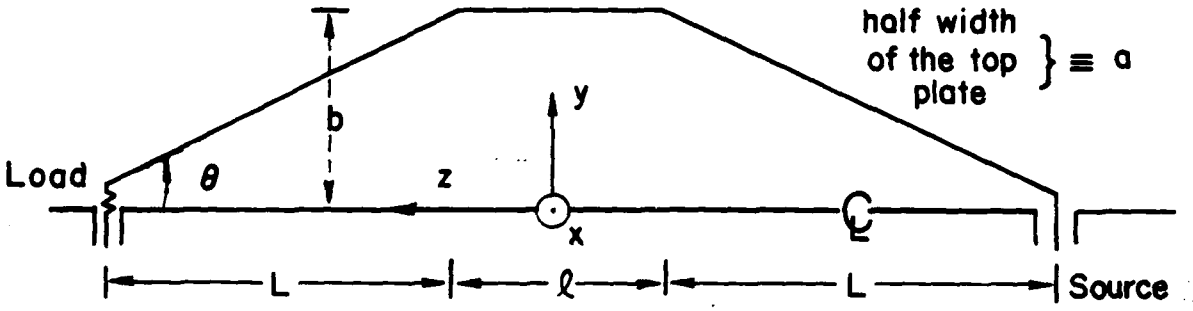

Figure 21. Geometry of a parallel-plate transmission line type of simulator.

TABLE 1. COMPARISON OF THE VALUES OF VARIOUS PARAMETERS FOR THE ALECS AND HARVARD'S MODEL SIMULATOR FACILITIES

Parameter	ALECS	Harvard's Model (October 1978)
ℓ	15.01 m	1.15 m
L	50.255 m	3.15 m
b	12.80 m	0.75 m
a	12.50 m	.875 m
θ	14.29°	13.39°
(b/a)	1.024	0.857
(L/b)	3.92617	4.2
$z_c^{(TEM)}$ (calc)	~90 Ω	~82 Ω

the axial component of the electric field couples to the resistors in the axial direction and some of the transverse electric field couples to the transverse resistors. It is desirable for such a modal filter to be away from the working volume to avoid its coupling with the test objects. Initially, one may think of locating such a modal filter in the output section, but not too close to the terminator, since non-TEM modes are evanescent there. Figure 22 shows the approximate location of the initial modal filter in the output transition and a possible second filter in the input transition, if required. Figure 16 of the earlier section illustrates the structural details of the modal filter. In any individual sheet, a two-dimensional array of resistors R_t and R_ℓ. Each resistive sheet conincides with a TEM equipotential and the stream functions for the configurations of the model simulator and ALECS are shown in Figures 17 and 23. The top plate is held at a potential V_o and the equipotentials are plotted in steps of 0.1 V_o and the stream functions in steps of 0.1 U_o. U_o is proportional to the total current flowing on half of the top plate. The equipotential contour coordinates are tabulated in Table 2. The resistive sheets along such equipotential surfaces are comprised of a two-dimensional array of resistors R_t and R_ℓ (see Figure 3). The initial values of these resistors can be evaluated from the following equations.

$$R_\ell \cong [Z_o \sin(\alpha)]/2 \tag{60}$$

$$R_t \cong Z_o/[2 \sin(\alpha)] \tag{61}$$

The above equations were derived earlier by viewing the resistive sheets as plane wave absorbers and letting a TM and TE wave become incident on the sheet at an angle α.

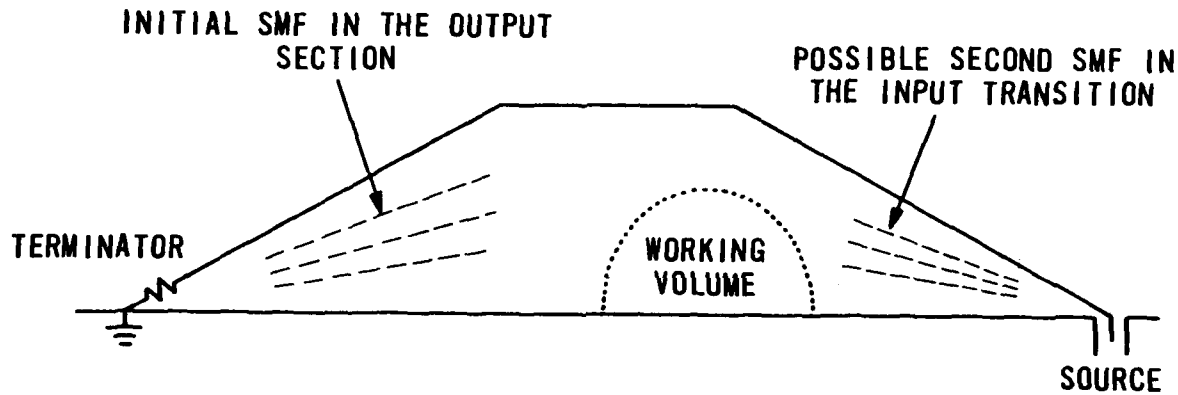

Figure 22. Side view of the simulator showing the approximate locations of two possible spatial model filters.

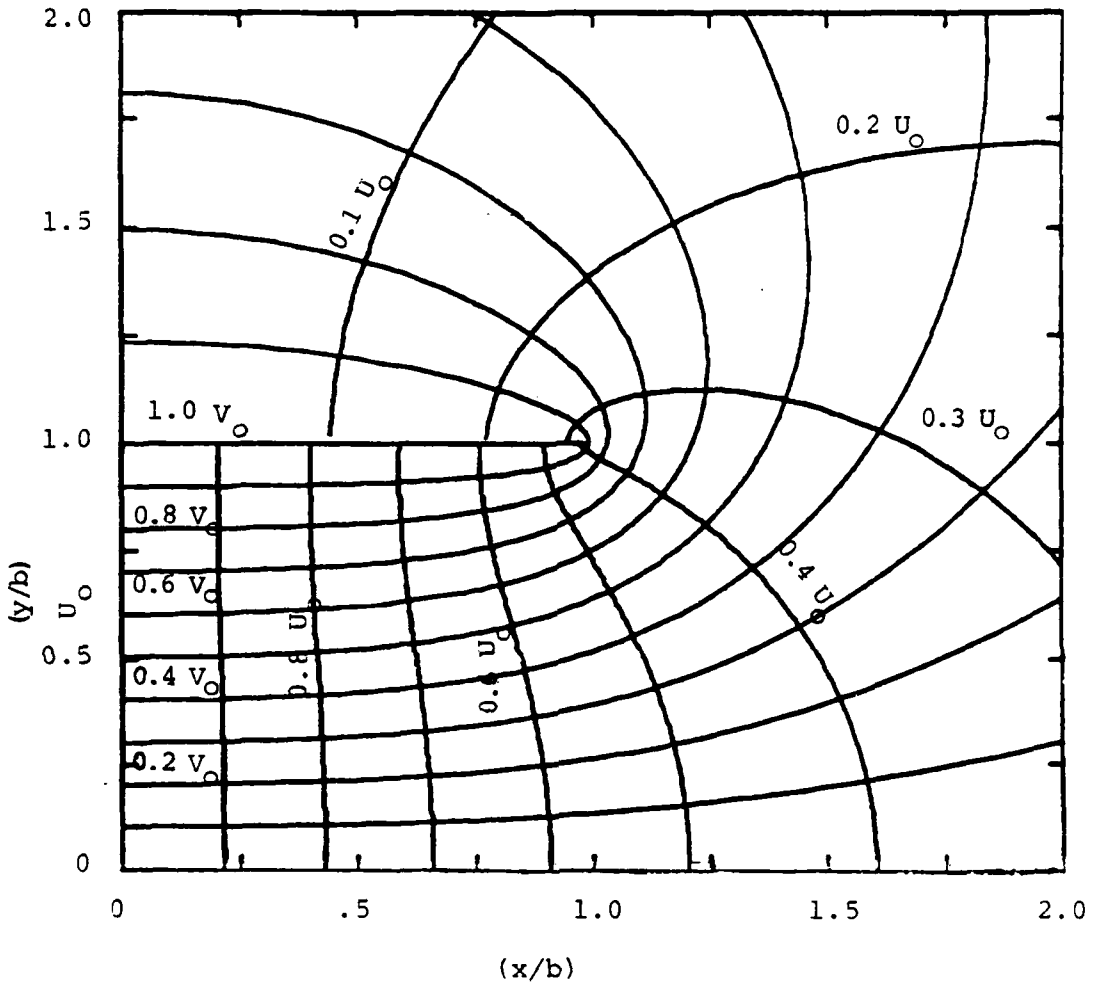

Figure 23 TEM equipotential and electric field lines in the conical transmission line of ALECS facility ((b/a) = 1.024 and (L/b) = 3.926; with a TEM characteristic impedance from top plate to ground plane of ∿ 90 Ω).

TABLE 2. EQUIPOTENTIAL CONTOUR COORDINATES (x/b,y/b)

0.1 V_o contour	
Model	ALECS
(0 .028,.100)	(0.026,.101)
(0.115,.100)	(0.105,.101)
(0.207,.100)	(0.190,.102)
(0.300,.101)	(0.276,.103)
(0.394,.102)	(0.362,.104)
(0.489,.103)	(0.450,.106)
(0.585,.104)	(0.539,.108)
(0.684,.107)	(0.631,.111)
(0.785,.110)	(0.725,.115)
(0.890,.114)	(0.826,.120)
(0.999,.119)	(0.930,.127)
(1.115,.126)	(1.042,.136)
(1.240,.137)	(1.164,.149)
(1.377,.151)	(1.299,.165)
(1.531,.170)	(1.452,.189)
(1.709,.198)	(1.631,.221)
(1.923,.238)	(1.847,.267)
(2.188,.299)	(2.117,.336)
(2.350,.340)	(2.281,.383)
(2.537,.392)	(2.472,.442)
(2.758,.459)	(2.698,.518)
(3.024,.548)	(2.972,.618)
(3.353,.666)	(3.310,.751)
(3.548,.741)	(3.512,.837)
(3.771,.831)	(3.743,.938)

0.2 V_o contour	
Model	ALECS
(0 .028,.200)	(0.026,.203)
(0.115,.200)	(0.105,.203)
(0.207,.201)	(0.189,.204)
(0.300,.202)	(0.274,.206)
(0.393,.203)	(0.360,.208)
(0.487,.206)	(0.447,.211)
(0.583,.209)	(0.535,.215)
(0.680,.213)	(0.626,.221)
(0.780,.219)	(0.719,.228)
(0.883,.226)	(0.816,.238)
(0.990,.236)	(0.917,.251)
(1.102,.250)	(1.025,.268)
(1.222,.270)	(1.140,.292)
(1.352,.296)	(1.267,.323)
(1.496,.332)	(1.407,.366)
(1.659,.383)	(1.567,.424)
(1.849,.456)	(1.745,.507)
(2.076,.563)	(1.978,.627)
(2.210,.635)	(2.109,.706)
(2.360,.725)	(2.256,.804)
(2.530,.837)	(2.422,.927)
(2.727,.980)	(2.612,1.082)
(2.955,1.165)	(2.831,1.280)
(3.084,1.278)	(2.953,1.401)
(3.224,1.409)	(3.085,1.540)

0.3 V_o contour	
Model	ALECS
(0.028,.300)	(0.026,.304)
(0.114,.300)	(0.104,.304)
(0.206,.301)	(0.188,.306)
(0.298,.303)	(0.272,.308)
(0.391,.305)	(0.357,.311)
(0.485,.308)	(0.443,.315)
(0.579,.312)	(0.529,.321)
(0.675,.318)	(0.618,.328)
(0.773,.325)	(0.708,.339)
(0.873,.336)	(0.801,.352)
(0.976,.350)	(0.898,.370)
(1.083,.369)	(0.998,.393)
(1.195,.395)	(1.105,.424)
(1.315,.430)	(1.218,.466)
(1.444,.478)	(1.340,.521)
(1.584,.545)	(1.474,.597)
(1.741,.639)	(1.623,.700)
(1.918,.772)	(1.789,.845)
(2.016,.859)	(1.879,.937)
(2.121,.964)	(1.975,1.049)
(2.233,1.092)	(2.076,1.182)
(2.352,1.249)	(2.181,1.343)
(2.477,1.442)	(2.288,1.539)
(2.542,1.555)	(2.342,1.652)
(2.607,1.682)	(2.395,1.777)

TABLE 2 (continued)

0.4 V_o	
Model	ALECS
(0.028,.400)	(0.025,.404)
(0.114,.400)	(0.103,.405)
(0.205,.401)	(0.186,.406)
(0.297,.403)	(0.269,.409)
(0.389,.406)	(0.353,.412)
(0.481,.409)	(0.437,.417)
(0.575,.414)	(0.522,.424)
(0.669,.421)	(0.608,.433)
(0.764,.430)	(0.695,.445)
(0.860,.442)	(0.783,.461)
(0.959,.458)	(0.873,.481)
(1.059,.480	(0.966,.508)
(1.163,.510)	(1.061,.543)
(1.269,.550)	(1.159,.590)
(1.381,.604)	(1.261,.651)
(1.496,.678)	(1.367,.733)
(1.617,.779)	(1.476,.841)
(1.743,.917)	(1.586,.986)
(1.806,1.005)	(1.640,1.077)
(1.869,1.109)	(1.692,1.181)
(1.930,1.230)	(1.741,1.302)
(1.987,1.373)	(1.783,1.442)
(2.036,1.541)	(1.817,1.603)
(2.057,1.636)	(1.829,1.692)
(2.074,1.738)	(1.837,1.787)

0.5 V_o	
Model	ALECS
(0.028,.499)	(0.025,.504)
(0.113,.500)	(0.102,.505)
(0.204,.501)	(0.184,.506)
(0.295,.503)	(0.266,.509)
(0.387,.505)	(0.349,.513)
(0.478,.509)	(0.431,.518)
(0.570,.514)	(0.514,.525)
(0.662,.521)	(0.597,.534)
(0.754,.531)	(0.680,.547)
(0.847,.544)	(0.764,.563)
(0.940,.561)	(0.847,.584)
(1.034,.583)	(0.931,.620)
(1.127,.614)	(1.015,.674)
(1.221,.654)	(1.098,.694)
(1.314,.709)	(1.180,.754)
(1.406,.781)	(1.259,.832)
(1.494,.878)	(1.333,.934)
(1.574,1.006)	(1.397,1.064)
(1.609,1.085)	(1.423,1.142)
(1.639,1.176)	(1.444,1.230)
(1.662,1.279)	(1.457,1.329)
(1.676,1.396)	(1.462,1.438)
(1.679,1.528)	(1.454,1.559)
(1.675,1.600)	(1.445,1.624)
(1.666,1.676)	(1.432,1.692)

0.6 V_o	
Model	ALECS
(0.028,.599)	(0.025,.603)
(0.113,.599)	(0.101,.604)
(0.203,.600)	(0.182,.605)
(0.294,.602)	(0.264,.608)
(0.384,.605)	(0.345,.612)
(0.475,.608)	(0.426,.617)
(0.565,.613)	(0.506,.623)
(0.655,.620)	(0.586,.632)
(0.745,.629)	(0.666,.644)
(0.834,.641)	(0.745,.659)
(0.922,.657)	(0.822,.679)
(1.009,.678)	(0.898,.704)
(1.094,.706)	(0.971,.737)
(1.175,.744)	(1.041,.779)
(1.252,.793)	(1.105,.833)
(1.322,.858)	(1.162,.901)
(1.382,.942)	(1.208,.987)
(1.426,1.050)	(1.237,1.094)
(1.440,1.115)	(1.233,1.156)
(1.447,1.188)	(1.245,1.225)
(1.446,1.268)	(1.237,1.299)
(1.434,1.358)	(1.220,1.380)
(1.410,1.455)	(1.192,1.466)
(1.393,1.507)	(1.173,1.511)
(1.371,1.560)	(1.152,1.557)

TABLE 2. (concluded)

0.7 V_o	
Model	ALECS
(0.028,.699)	(0.025,.702)
(0.112,.699)	(0.100,.703)
(0.203,.700)	(0.181,.704)
(0.293,.701)	(0.261,.706)
(0.383,.703)	(0.341,.709)
(0.472,.706)	(0.421,.713)
(0.561,.711)	(0.500,.719)
(0.650,.716)	(0.578,.727)
(0.737,.724)	(0.654,.737)
(0.823,.734)	(0.729,.749)
(0.907,.748)	(0.801,.766)
(0.988,.766)	(0.869,.787)
(1.064,.789)	(0.934,.814)
(1.136,.820)	(0.992,.848)
(1.199,.860)	(1.042,.892)
(1.252,.912)	(1.081,.946)
(1.290,.978)	(1.107,1.012)
(1.308,1.062)	(1.113,1.092)
(1.308,1.110)	(1.108,1.138)
(1.300,1.164)	(1.096,1.187)
(1.283,1.222)	(1.076,1.240)
(1.256,1.285)	(1.047,1.295)
(1.218,1.353)	(1.010,1.353)
(1.194,1.388)	(0.987,1.383)
(1.167,1.423)	(0.962,1.413)

0.8 V_o	
Model	ALECS
(0.028,.798)	(0.025,.801)
(0.112,.799)	(0.100,.801)
(0.202,.799)	(0.180,.802)
(0.292,.800)	(0.260,.804)
(0.382,.802)	(0.339,.806)
(0.471,.804)	(0.418,.809)
(0.559,.807)	(0.495,.813)
(0.646,.811)	(0.571,.819)
(0.732,.817)	(0.645,.826)
(0.815,.824)	(0.717,.835)
(0.895,.834)	(0.785,.847)
(0.972,.847)	(0.848,.862)
(1.042,.864)	(0.906,.882)
(1.106,.886)	(0.955,.906)
(1.159,.914)	(0.995,.936)
(1.199,.950)	(1.022,.973)
(1.222,.996)	(1.033,1.018)
(1.223,1.052)	(1.025,1.071)
(1.213,1.084)	(1.012,1.100)
(1.196,1.119)	(0.993,1.132)
(1.170,1.156)	(0.966,1.165)
(1.135,1.196)	(0.933,1.199)
(1.090,1.238)	(0.891,1.235)
(1.063,1.259)	(0.867,1.253)
(1.034,1.281)	(0.841,1.271)

0.9 V_o	
Model	ALECS
(0.028,.898)	(0.025,.900)
(0.112,.899)	(0.100,.900)
(0.203,.899)	(0.180,.901)
(0.293,.900)	(0.260,.901)
(0.382,.900)	(0.339,.903)
(0.471,.902)	(0.417,.904)
(0.559,.903)	(0.493,.906)
(0.645,.905)	(0.568,.909)
(0.730,.908)	(0.641,.913)
(0.811,.912)	(0.710,.918)
(0.890,.918)	(0.776,.924)
(0.963,.924)	(0.836,.932)
(1.030,.933)	(0.889,.942)
(1.088,.945)	(0.933,.955)
(1.135,.959)	(0.967,.970)
(1.167,.978)	(0.986,.989)
(1.181,1.001)	(0.989,1.012)
(1.171,1.029)	(0.972,1.038)
(1.156,1.045)	(0.955,1.052)
(1.133,1.062)	(0.932,1.067)
(1.102,1.080)	(0.902,1.083)
(1.063,1.099)	(0.865,1.100)
(1.015,1.119)	(0.822,1.117)
(0.987,1.129)	(0.798,1.125)
(0.957,1.139(	(0.771,1.134)

With reference to Figure 24, a typical value of α is estimated by using

$$\alpha_t \simeq (\theta/2) + \arctan\left\{\frac{(2/3)\ L \tan(\theta/2)}{(4/3)\ L + \ell}\right\} \qquad (62)$$

Substituting for various parameters from Table 1, gives

(a) ALECS facility

$$\theta = 14.29°; \quad L = 50.255 \text{ m}; \quad \ell = 15.01 \text{ m}$$

$$\alpha_t \simeq 7.15° + \arctan(4.2/82)$$

$$\simeq 10.1° \qquad (63)$$

(b) Harvard's model simulator

$$\theta = 13.39°; \quad L = 3.15 \text{ m}; \quad \ell = 2.15 \text{ m}$$

$$\alpha_t \simeq 6.7° + \arctan(0.25/5.35)$$

$$\simeq 9.4° \qquad (64)$$

Since the value of α_t is approximately the same for both ALECS and the model simulator, the following values of the resistors can apply to both structures. Using an α_t of 10° in Equations (60) and (61),

$$R_\ell \simeq 60\pi \times \sin(10°) \simeq 33\ \Omega \qquad (65a)$$

$$R_t \simeq 60\pi / \sin(10°) \simeq 1085\ \Omega \qquad (65b)$$

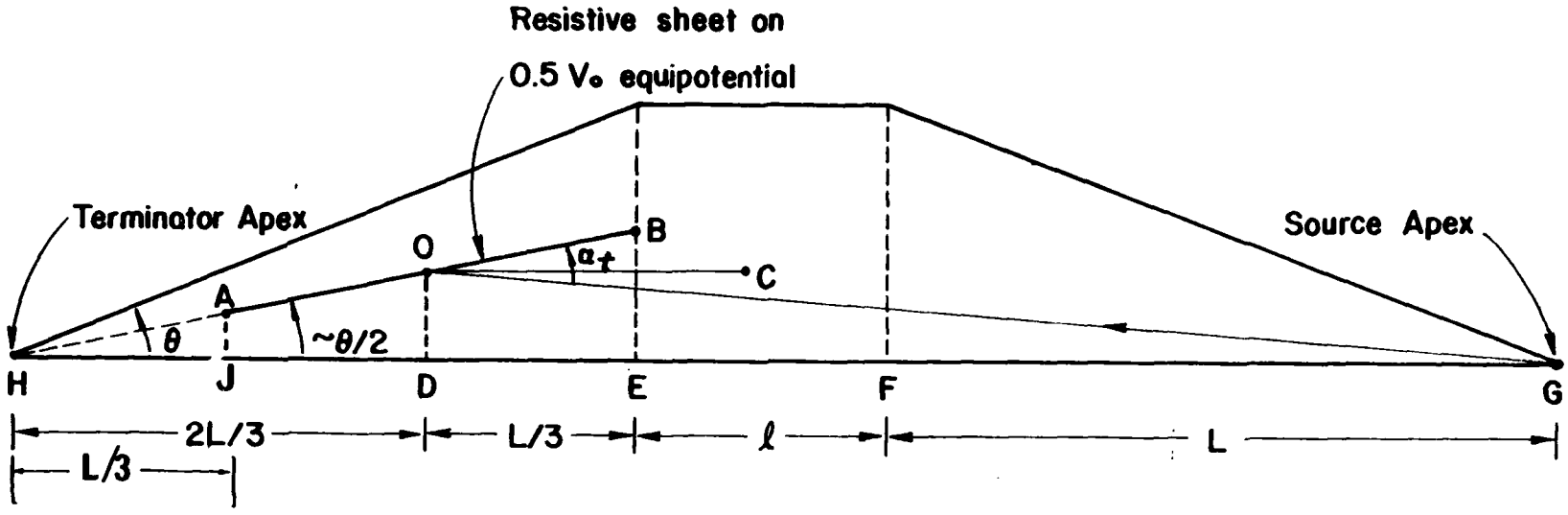

Note $\alpha_t = B\hat{O}G = B\hat{O}C + C\hat{O}G \simeq (\theta/2) + C\hat{O}G = (\theta/2) + O\hat{G}D$

$$\simeq (\theta/2) + \text{Arctan}\,(OD/DG)$$

$$\simeq (\theta/2) + \text{Arctan}\left[\frac{(2/3)L\,\tan\,(\theta/2)}{(4/3)L + \ell}\right]$$

Figure 24. Geometry for estimating a typical value of α ($\cong \alpha_t$).

These resistor values provide a starting point in the experimental optimization which will eventually lead to an optimum modal filter.

2. FABRICATION OF THE MODEL MODAL FILTER

Initially it is considered useful to fabricate a single resistive sheet that can be placed on the $0.5\ V_o$ equipotential surface shown in Figure 25. A dielectric support structure will also be required. The sheet will be roughly 1.5 m long and 3 m wide suspended in the output transition region along the $0.5\ V_o$ equipotential surface. The sheet will consist of a grid of about 8 cm × 8 cm of wires with 0.5 W resistors. The unit cell size Δ_t will reduce as one moves towards the terminator, whereas Δ_ℓ is less constrained and can be kept constant. To begin with R_t can be absent (= infinity) and only R_ℓ can be varied for evaluating its effect on the TM mode of propagation. Note that the longitudinal resistors carry the TM mode currents. Later R_t can be included if required. Since the power levels involved in the output section of the model simulator are low, energy dissipation in the resistors is not a serious problem.

In the ALECS facility, the dielectric support structure has to be mechanically rigid and the resistors may have to be placed in plasic tubes containing oil.

3. EXPERIMENTAL EVALUATION

Some experimental procedures useful in evaluating the filter performance are listed below. The fields in the working volume will be monitored in each configuration.

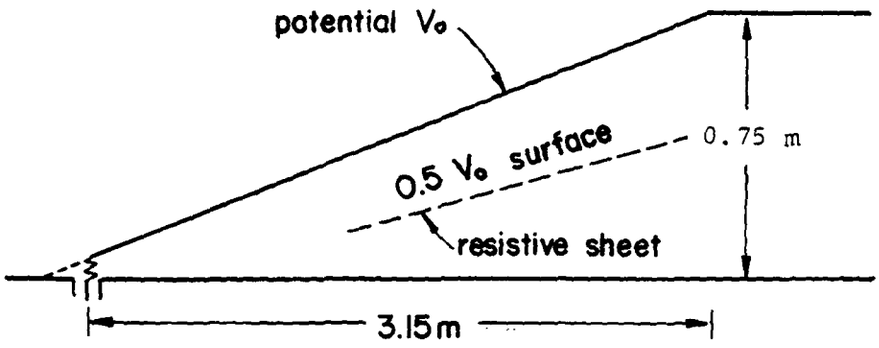

(a) Side view of the output section

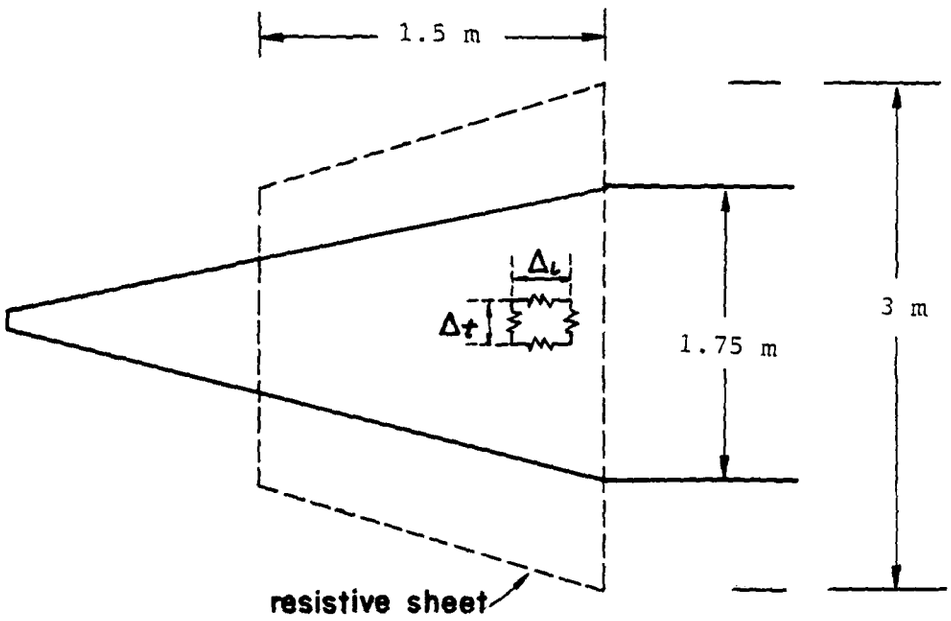

(b) Top view of the output section

Figure 25. Approximate location of the output resistive sheet for initial experiments.

- set up the dielectric support structure
- add the $0.5\ V_o$ sheet
  (a) uniform resistors, using various combinations of R_ℓ and R_t centered around $R_\ell \simeq 33$ ohms, $R_t \simeq 1100$ ohms, and others where most damping occurs
  (b) nonuniform resistors
- remove $0.5\ V_o$ sheet and add $0.3\ V_o$ and $0.7\ V_o$ and repeat the field monitoring
- add more sheets as needed for improved and optimum damping

One limitation with the performance of the modal filter is the initial reflection off the front edge of the filter. If, indeed, this proves to be a serious problem in preliminary experimentation, a suitable gradient will be considered in the resistor values with high values near the front edge and gradually decreasing as one moves towards the terminator.

4. POTENTIAL BENEFITS

The chief benefit from introducing the modal filter is the suppression or removal of energy from the non-TEM modes with negligible effect on the TEM mode of propagation.

At lower frequencies, the dominant mode is the TEM mode, and the modal filter does not disturb the quality of simulation. But in the intermediate frequency regime, where the non-TEM modes get excited, the modal filter is expected to be effective after careful experimental optimization. At high frequencies, where ray-optic considerations apply, energy is still removed because of multiple passes through the filter. This results in reduced high frequency ripple which has been experimentally observed in the past (Ref. 21).

The next section discusses the experimental work performed to date concerning the mode suppression.

VII. EXPERIMENTAL RESULTS

The experimental results that led to the decomposition of the measured fields at the two frequencies (626 MHz and 264 MHz) into TEM and TM_{0n} modes were reported earlier in Section II. Note that the 264 MHz frequency on the model simulator corresponds to the 25 MHz notch frequency for the principal magnetic field in the ALECS facility. The notch has been analyzed and understood to be the result of standing wave distribution owing to the reflections of both TEM and TM_{0n} modes. In the case at hand, i.e., at 264 MHz, the only higher order mode is the TM_{01} mode. A similar notch in the principal electric field was found at 271 MHz. This notch when analyzed also led us to conclude that the only higher order mode is the TM_{01} mode. The principal electric field component E_y for the TEM and TM_{01} modes are shown in Figures 26 and 27 for two different terminator locations. The real and imaginary parts of E_{yTEM} are shown at the top of Figures 26 and 27. Both maximum/minimum ratios are quite comparable with each other and the very large second ratio is due to the very deep second minimum, indicating that at this frequency, the TEM wave is not properly terminated. Note that the frequency is such that the simulator plate separation is about one wavelength and, hence a simple transmission line theory does not hold at this frequency. Along with the axial E_{zTM}, which characterizes the TM_{01} mode, the bottom part of Figures 26 and 27 also show the vertical E_{yTM} field. The real part of E_{yTM} is very small compared with the real parts of E_y and E_{yTEM} and has been omitted. However, of great interest is the imaginary part of E_{yTM}. Although substantially smaller than the imaginary part of E_{yTEM}, it can be so present in the standing wave pattern as to be almost equal and opposite to the imaginary part of E_{yTEM} precisely

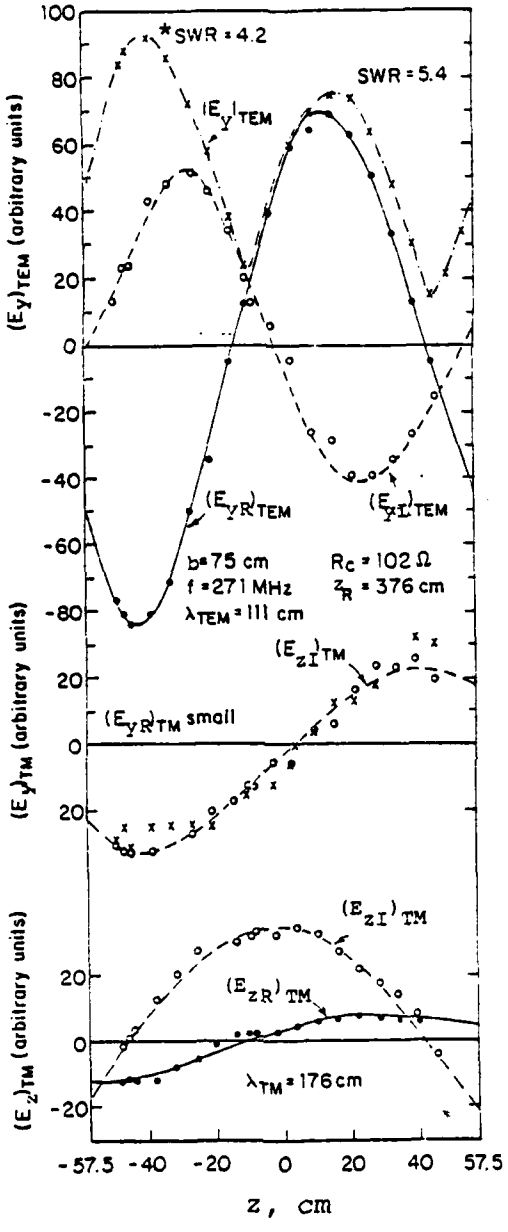

Figure 26. TEM and TM components of the electric field in the parallel plate region.

* The abbreviation SWR is used to mean standing wave ratio.

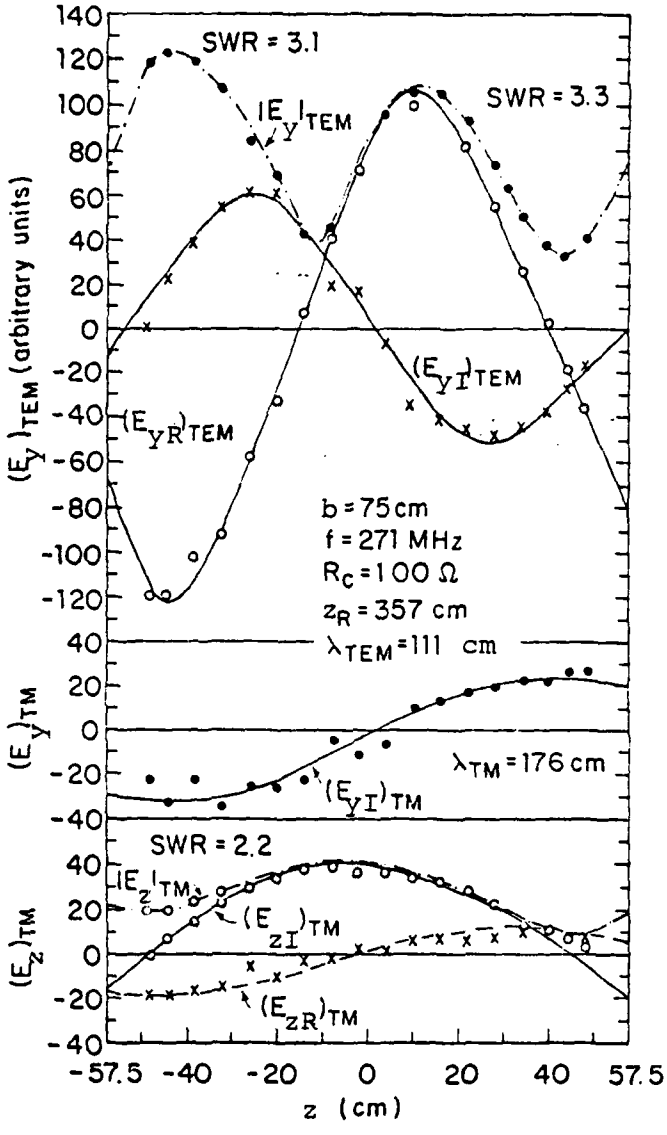

Figure 27. TEM and TM components of the electric field in the parallel-plate region.

where the real part of E_{yTEM} is zero. When this occurs, a very deep minimum in the total field $|E_y|$ is produced at this location much like the 25 MHz magnetic field notch in ALECS.

Next, attempts were made to reduce the deep standing wave minimum. The initial value of lumped resistor network from the earlier section was tried and it had no significant effect on the minimum. This is not surprising because of the approximations made in those calculations. What is required is a careful experimental optimization of the resistor network values. However, it is somewhat cumbersome to make experimental evaluations while changing the resistor values. A theoretical analysis has shown that a correctly designed, continuous, thin resistive sheet located half-way between the plates of a parallel-plate region can reduce the reflected TM mode to negligible magnitudes. Recent experimental results, unavailable for reporting at this time, have indicated that such a sheet with impedance of about 200 Ω can significantly reduce the standing wave ratio (from 27 without the sheet to ∿ 5 with the sheet) at the notch frequency. If a resistive sheet is effective, it is reasonable to expect that a lumped resistor network whose unit cell size is small compared to wavelength will also be effective. The criterion to decide whether the sheet or lumped resistors be used, should be based on practical considerations, i.e., which is easier to implement in the ALECS facility? It is true that it has not yet been experimentally demonstrated that a lumped resistor network can have the same effect as a resistive sheet. Also, the possibility of introducing more than one sheet much like the configuration illustrated in Figure 22 needs to be investigated. It was communicated by Harvard investigators that a single sheet of 200 Ω can reduce the TM_{01} mode by about 25 percent, indicating that more than one sheet can damp out the TM_{01} mode by making multiple bounces possible.

Another interesting way of reducing the deep minimum has also been experimentally demonstrated by using a folded or a sleeve section near the top plate as shown in Figure 28. The sleeve is a trapezoidal plate located parallel to and 5 cm below the top plate in the output section and has an open end toward the parallel-plate region and a closed end toward the load. The length is $\lambda_{TEM}/4$ and is equivalent to an open end toward the load with a length of $\lambda_{TEM}/2$. The standing wave in the diagram at the upper left of Figure 28 was measured at the notch frequency of 271 MHz before the folded section was inserted. The deep minimum occurs with an associated SWR of 24. With the folded section inserted with its open end at the junction of the parallel-plate region and the triangular plate (s = 0) and its closed end at a distance s = 35 cm from this junction, the standing-wave pattern shown in the middle figure at the top was obtained. Evidently, the notch has been shifted from the second to the first minimum. By lengthening the folded section so that, with its open end at s = 0, the closed end is at s = 45 cm, the notch is shifted back to the second minimum.

The four diagrams in the lower half of Figure 29 were all measured with the folded section located with its open end at s = 5 cm from the parallel-plate/triangular-plate junction at s = 0 and its closed end at s = 32.5 cm so its interior length is 27.5 cm = $\lambda_{TEM}/4$. The four graphs are for the frequencies f = 260, 271, 350, and 400 MHz. It is seen that no deep minima occur and the SWR is quite low throughout. The SWR at f = 200 MHz was 1.7, at f = 450 MHz it was 2.6. It may be concluded from these preliminary measurements that a folded section or sleeve of proper length and location can greatly decrease the SWR over a wide range of frequencies about the notch frequency, as well as completely eliminate the notch.

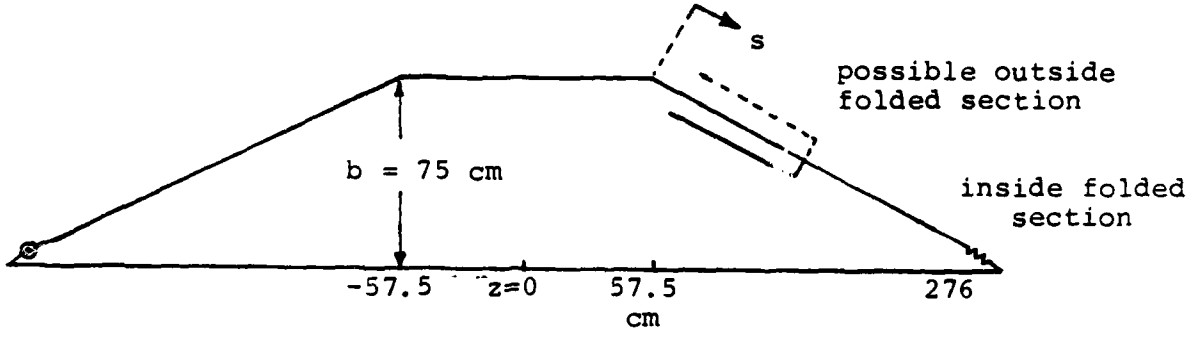

Figure 28. Cross section of Harvard simulator with sleeve or apron sections.

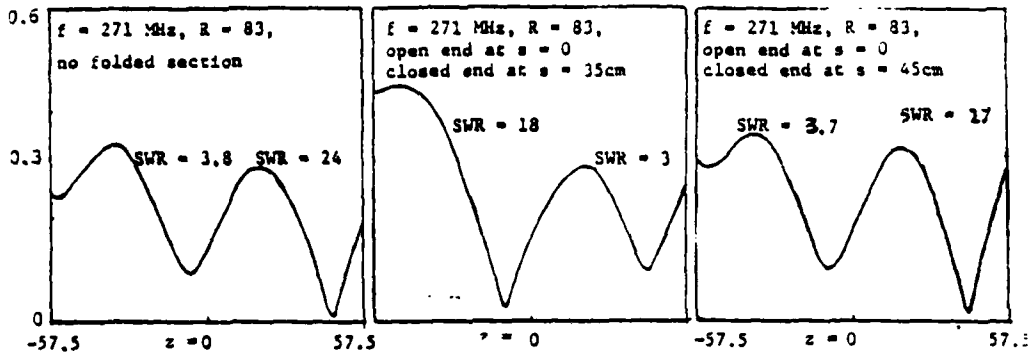

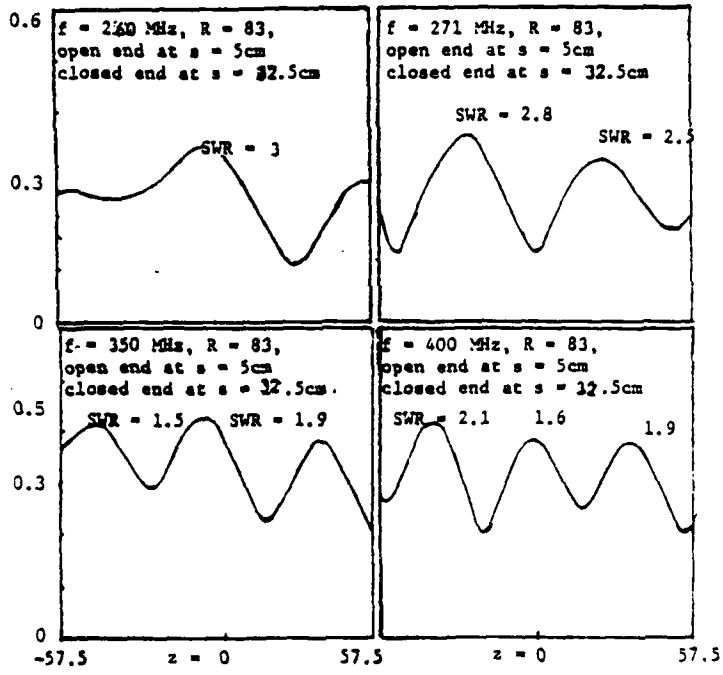

Figure 29. Measured field in parallel plate region with and without the folded section.

The measurements reported above were made with a high-conducting metal sleeve or folded section - a purely reactive device that corrects the phase of the reflected wave. Future measurements will add dissipation to the folded section to, hopefully, decrease further the reflected amplitude by absorption as well as by selective reflection.

Experiments are currently in progress at the time of writing this report to reach the optimum structure for modal suppression. Several structures have been shown to be effective, and what remains to be done is a careful optimization procedure.

VIII. SUMMARY

A two-parallel-plate transmission-line type of EMP simulator has been historically employed to propagate an electromagnetic pulse with a plane wavefront. Since the pulse consists of a wide frequency spectrum, the structures that nave been built propagate modes other than the principal TEM mode. Consequently, techniques of non-TEM mode suppression is an important element in the advancement of simulator technology. This section addresses the problem of mode suppression and, in particular, the electromagnetic considerations of a volumetric suppressor. This suppressor is the result of one of several techniques of mode suppression. Empirical relations are developed for computing the resistor values required in the fabrication by viewing the suppressor as a plane wave absorber.

An important feature of the SMF is its location. Figure 22 shows the side view of a parallel-plate EMP simulator, indicating the approximate locations of two possible SMF. The SMFs have to be located away from the two apexes where the non-TEM modes are evanescent. It is also essential to place the SMF so as to minimize any coupling effects with the test object.

To date, several structures have been experimentally attempted, including (a) lumped resistor network, (b) single vertical resistor, (c) metal plate in the middle of the output conic section, (d) folded section near the top plate in the output section, and (e) a single resistive sheet. The results of a single resistive sheet have yielded a significant reduction in the deep minimum. Some of the experiments for the future include introducing more than one sheet for improved suppression of TM modes via multiple bouncing, and investigations on how well lumped resistors can simulate continuous sheets. These experiments are being pursued at Harvard

University on the model simulator, under a related research effort. Owing to these considerations, firm recommendations on the modifications to be implemented in the ALECS facility cannot be made at this time. However, the work to date has clearly demonstrated that selective modal suppression in this class of simulators is possible and is effective in improving the overall simulator performance.

Finally, although present interest is in EMP simulators, it is recognized that the mode suppression considerations presented herein are fairly general and can apply to other types of multimoded structures (e.g., TEM cell) where the non-TEM modes are also undesirable, and due to the lack of radiation losses can cause even more severe problems.

REFERENCES

Note that the Sensor and Simulation Notes, Miscellaneous Simulator Memos and the Interaction Notes referenced below are edited by Dr. Carl E. Baum of AFWL/NTYEE.

1. L. Marin, "Modes on a Finite-Width, Parallel-Plate Simulator: I. Narrow Plates", Sensor and Simulation Note 201, September 1974.

2. C-M. Chu, "Mathematics of Guided Wave Propagation in Open Structures", Sensor and Simulation Note 206, May 1974.

3. T. Itoh and R. Mittra, "Analysis of Modes in a Finite-Width Parallel-Plate Waveguide", Sensor and Simulation Note 208, January 1975.

4. L. Marin, "Modes on a Finite-Width, Parallel-Plate Simulator: II. Wide Plates", Sensor and Simulation Note 223, March 1977.

5. L. Marin and G.C. Lewis, "Modes on a Finite-Width Parallel-Plate Simulator: III. Numerical Results for Modes on Wide Plates", Sensor and Simulation Note 227, September 1977.

6. A.E.H. Love, "Some Electrostatic Distributions in Two Dimensions", Proc. London Math. Soc., Vol. 22, pp. 337-369, 1923.

7. C.E. Baum, "Impedance and Field Distributions for Parallel-Plate Transmission-Line Simulators", Sensor and Simulation Note 21, June 1966.

8. T.L. Brown and K.D. Granzow, "A Parameter Study of Two-Parallel-Plate Transmission-Line Simulators of EMP Sensor and Simulation Note 21", Sensor and Simulation Note 52, April 1968.

9. C.E. Baum, D.V. Giri and R.D. González, "Electromagnetic Field Distribution of the TEM Mode in a Symmetrical Two-Parallel-Plate Transmission Line", Sensor and Simulation Note 219, 1 April 1976.

10. F.C. Yang and K.S.H. Lee, "Impedance of a Two-Conical-Plate Transmission Line", Sensor and Simulation Note 221, November 1976.

11. F.C. Yang and L. Marin, "Field Distributions on a Two-Concial-Plate and a Curved Cylindrical-Plate Transmission Line", Sensor and Simulation Note 229, September 1977.

12. C.E. Baum, "The Conical Transmission Line as a Wave Launcher and Terminator for a Cylindrical Transmission Line", Sensor and Simulation Note 31, January 1967.

13. C.E. Baum, "General Principles for the Design of ATLAS I and II, Part V: Some Approximate Figures of Merit for Computing the Waveforms Launched by Imperfect Pulser Arrays onto TEM Transmission Lines", Sensor and Simulation Note 148, 9 May 1972.

14. F.C. Yang, "Discrete and Continuous Spectra of Finite Width Parallel-Plate Simulator's Field", Sensor and Simulation Note 262, June 1979.

15. D.V. Giri, C.E. Baum, R.W.P. King, D.J.Blejer and S-K. Wan, "Experimental Investigations into Higher-Order Mode Effects and Simulator/Object Interaction in Parallel-Plate Transmission-Line Geometries", Miscellaneous Simulator Memo 11, 26 May 1977.

16. C.E. Baum, "The Diffraction of an Electromagnetic Plane Wave at a Bend in a Perfectly Conducting Planar Sheet", Sensor and Simulation Note 47, 9 August 1967.

17. J.B. Keller and A. Blank, "Diffraction and Reflection of Pulses by Wedges and Corners", Comm. on Pure and Applied Math., Vol. 4, p. 75, 1951.

18. D.F. Higgins, "The Diffraction of an Electromagnetic Plane Wave by Interior and Exterior Bends in a Perfectly Conducting Sheet", Sensor and Simulation Note 128, January 1971.

19. K.K. Chan, L.B. Felsen, S.T. Peng and J. Shmoys, "Diffraction of the Pulsed Field from an Arbitrarily Oriented Electric or Magnetic Dipole by a Wedge", Sensor and Simulation Note 202, October 1973.

20. D.L. Endsley and D.B. Westenhaver, "Special Report on Field Measurements", ALECS Memo 4, 28 December 1967.

21. J.C. Giles, M.K. Bumgardner, G. Seely and J. Furaus, "Evaluation and Improvement of the CW Performance of the ALECS Facility," ALECS Memo 10, Volume I, Technical Discussion, September 1975.

22. T.T. Wu, R.W.P. King, D.J. Blejer and S-K. Wan, "Laboratory Model Parallel-Plate Transmission-Line Type of EMP Simulator (Description of the Set-up and Sample Measurements)," Miscellaneous Simulator Memo 16, 31 July 1977.

23. M. Krook, R.W.P. King, D.J. Blejer, T.K. Sarkar and S-K Wan, "The Electric Field in a Model Parallel-Plate EMP Simulator at a High CW Frequency," Miscellaneous Simulator Memo 17, July 1978.

24. D.V. Giri, T.K. Liu, F.M. Tesche and R.W.P. King, "Parallel-Plate Transmission-Line Type of EMP Simulators: A Systematic Review and Recommendations", Sensor and Simulation Note 261, 1 April 1980.

25. D.V. Giri, C.E. Baum, C.M. Wiggins, W.O. Collier and R.L. Hutchins, "An Experimental Evaluation and Improvement of the ALECS Terminator", ALECS Memo 8, 8 May 1977.

26. N. Marcuvitz, Waveguide Handbook, p. 64, McGraw-Hill Book Company, New York, 1951.

27. A.M. Rushdi, R.C. Mendez, R. Mittra and S.-W. Lee, "Leaky Modes in Parallel-Plate EMP Simulators", IEEE Trans. Electromagnetic Compatibility, vol. EMC-20, pp. 443-453, 1978.

28. C.E. Baum, "Interaction of Electromagnetic Fields with an Object Which has an Electromagnetic Symmetry Plane", Interaction Note 63, 3 March 1971.

29. M.L. Crawford, "Generation of Standard EM Fields Using TEM Transmission Cells", IEEE Trans. on Electromagnetic Compatability, Vol. EMC-16, pp. 189-195, November 1974.

30. M.L. Crawford, J.L. Workman and C.L. Thomas, "Generation of EM Susceptibility Test Fields Using a Large Absorber-Loaded TEM Cell", IEEE Trans. on Instrumentation and Measurement, Vol. IM-26, No. 3, pp. 225-230, September 1977.

31. M.L. Crawford, J.L. Workman and C.L. Thomas, "Expanding the Bandwidth of TEM Cells for EMC Measurements", EMC-20, No. 3, pp. 368-375, August 1978.

32. D.V. Giri and C.E. Baum, "Spatial Modal Filters for Suppression of Non-TEM Modes in Parallel-Plate Simulators", presented at the Nuclear EMP Meeting held at the University of New Mexico and sponsored by IEEE Albuquerque Joint Chapters (AP-S, MTT-S, EMC-S) and the Department of Electrical Engineering and Computer Science, University of New Mexico, 6-8 June 1978.

33. B.K.Singaraju,D.V.Giri and C.E.Baum, "Further Developments in the Application of Contour Integration to the Evaluation of the Zeros of Analytic Functions and Relevant Computer Programs", Mathematics Note 42, March 1976.